



Norwegian University of
Science and Technology

Finite Element Modeling of Heat Generation in 1-3 Piezocomposite Transducers for Underwater Ultrasonic Applications

Lars Erik Myrstuen

Master of Science in Physics and Mathematics

Submission date: June 2018

Supervisor: Jon Andreas Støvneng, IFY

Co-supervisor: Lars Hoff, Høgskolen i Sørøst-Norge
Marcus Wild, Høgskolen i Sørøst-Norge

Norwegian University of Science and Technology
Department of Physics

Preface

This thesis was written in 2018 during the final semester of my master's degree in Applied Physics and Mathematics at the Norwegian University of Science and Technology (NTNU). The work was conducted in cooperation with the University of South-Eastern Norway (USN). The last two sections of the second chapter are based on my specialization project *Thermal analysis of electronics for space applications* completed during the preceding semester. I would like to thank my supervisors Prof. Lars Hoff and PhD student Marcus Wild at the University of South-Eastern Norway for the discussions and guidance provided during our weekly meetings.

Lars Erik Myrstuen
Horten, Norway
June, 2018

Abstract

Today, piezoelectric ultrasound transducers are used extensively for underwater applications such as sonar. In such transducers, operating in thickness mode, the active part is often a 1-3 piezocomposite, usually made of lead-zirconate-titanate rods embedded in a passive polymer/epoxy matrix. One or several matching layers can be connected to the piezocomposite for increased acoustic transmission into water. Upon electrical and/or mechanical excitation, the transducer will heat up due to mechanical, dielectric and piezoelectric losses.

In this thesis, the heat generation in 1-3 piezocomposite transducers was investigated following three steps. First, the heat generation in 1-3 piezocomposites due to material energy loss mechanisms was investigated through the use of the finite element method for varying lead-zirconate-titanate volume fractions and square lateral rod sizes. For both composite materials, the losses were represented through complex material coefficients. The composites were electrically excited by a sinusoidal voltage. The simulations were built in the COMSOL Multiphysics software and run over frequency intervals extending over the fundamental thickness resonance and anti-resonance frequency of the composites.

Second, one of the composites was connected to a quarter-wavelength matching layer with losses incorporated through complex material coefficients. A water load was applied to the front face of the matching layer.

Finally, the resultant spatial heat generation was used as the heat source in a steady-state heat transfer model of the same structure. A constant temperature boundary condition was applied to the interface between the matching layer and water load, and convective heat transfer between an air backing layer and the composite was assumed. It was found that the resultant spatial temperature distribution was homogeneous in planes normal to the thickness direction to a very high degree, both in the composite and in the matching layer. Using a peak voltage of 200 V, a maximum temperature rise of approximately 24 °C was obtained.

Sammendrag

Piezoelektriske ultralydtransdusere blir i dag benyttet i et stort omfang til undervannsformål som sonar. I slike transdusere, som opererer rundt resonans i tykkelsesretningen, er den aktive delen ofte en 1-3-piezokompositt. Denne består vanligvis av piezoelektriske staver laget av blyzirkon-titanat innkapslet i en polymer-/epoxy-matrise. Ett eller flere match-lag kan kobles til 1-3-piezokompositten for forbedret akustisk transmisjon inn i vannet. Når piezokomposittene utsettes for mekanisk og/eller elektrisk spenning, vil dette resultere i varmeutvikling som følge av mekaniske, dielektriske og piezoelektriske tap.

I denne masteroppgaven ble varmeutviklingen i 1-3-piezokompositt-transdusere undersøkt i tre steg. Først ble varmeutviklingen i 1-3-piezokompositter som følge av de nevnte tapsmekanismene undersøkt ved bruk av endelig element metoden for ulike volumfraksjoner av blyzirkon-titanat og kvadratiske laterale stavdimensjoner. Tapene i begge komposittmaterialene ble representert gjennom komplekse materialkoeffisienter. Komposittene ble utsatt for en vekselspenning. Simuleringene ble utført i programvaren COMSOL Multiphysics og foretatt over frekvensintervall som dekket den fundamentale resonansen og antiresonansen i tykkelsesretningen.

Deretter ble én av komposittene koblet til et match-lag med tap innført ved komplekse materialkoeffisienter. Den øvre overflaten ble belastet med vann.

Til slutt ble den resulterende romlige varmeutviklingen brukt som varmekilde i en stasjonær varmestrømsimulering av den samme strukturen. En grensebetingelse med konstant temperatur ble tillagt grenseflaten mellom match-laget og vannet, og varmetransport ved konveksjon mellom luften i baklaget og baksiden av kompositten ble antatt. Den resulterende temperaturfordelingen var i høy grad homogen i plan normalt på tykkelsesretningen, både i kompositten og i match-laget. Med en spenningsamplitude på 200 V var den maksimale temperaturøkningen 24 °C.

Contents

1	Introduction	6
2	Theoretical background	9
2.1	Wave propagation in linear elastic materials	9
2.1.1	Linear elastic materials	9
2.1.2	The elastic wave equation	11
2.1.3	One-dimensional propagation of pressure waves in a free medium	12
2.1.4	Reflections on boundaries between semi-infinite and finite-sized media	13
2.1.5	Losses	13
2.2	Piezoelectricity	15
2.2.1	Linear dielectrics	15
2.2.2	The piezoelectric effect	16
2.2.3	Piezoelectric ceramics	18
2.2.4	Power dissipation density	19
2.2.5	Losses in dielectrics and piezoelectrics	22
2.3	1-3 piezocomposites	23
2.3.1	Materials and composition	23
2.3.2	Resonances	25
2.3.3	The effective medium model for thickness-model oscil- lations in 1-3 piezocomposites	27
2.3.4	Ohm's law and the Joule heating law	33
2.4	Heat transfer	34
2.4.1	Fourier's law	34
2.4.2	The heat equation	35
2.5	Finite element method	35
3	Method: FEM modeling	38
3.1	Unit cell modeling	38
3.2	1-3 piezocomposites in vacuum	41
3.2.1	Dimensions of the unit cells	41
3.2.2	Materials and losses	41
3.2.3	Boundary conditions	43

3.2.4	Meshing considerations	44
3.2.5	Determination of sampling frequency and frequency domain	46
3.2.6	Physical quantities of interest	47
3.3	1-3 piezocomposite with electrodes, matching layer and water load	51
3.3.1	Dimensions of the unit cell	51
3.3.2	Materials and losses	52
3.3.3	Boundary conditions and related assumptions	54
3.3.4	Meshing considerations	55
3.3.5	Physical quantities of interest	55
3.4	Steady-state heat transfer	56
3.4.1	Boundary conditions and related assumptions	56
4	Results	58
4.1	1-3 composites in vacuum	59
4.2	1-3 composite with electrodes, matching layer and water load .	68
4.3	Steady-state heat transfer in 1-3 composite with electrodes, matching layer and water load	75
5	Discussion	80
5.1	1-3 composites in vacuum	80
5.2	1-3 composite with electrodes, matching layer and water load .	83
5.3	Steady-state heat transfer in 1-3 composite with electrodes, matching layer and water load	86
6	Conclusion	89
A	Piezoelectric equations and interrelations	91
B	Material properties	93
	References	96

Chapter 1

Introduction

The piezoelectric effect was discovered in 1880 by Jacques and Pierre Curie [1]. They found that crystals such as quartz were electrically polarized under applied mechanical stresses and mechanically deformed under application of an electric field. The former effect is called the direct piezoelectric effect and the latter, the inverse piezoelectric effect [2].

In the 1950s, the modern era of piezoelectric transducers began with the discovery of the strong piezoelectric effect in lead-zirconate-titanate ceramics, also known as PZTs. Today, it is still being used extensively in piezoelectric ultrasonic transducers, which convert the energy of sound waves propagating at frequencies beyond the human hearing threshold, to electrical signals and vice versa. Typical applications are medical diagnostics, SONAR (SOund Navigation And Ranging) and underwater communication.

A common problem when PZT is used in ultrasonic transducers for medical or underwater applications is the significant characteristic acoustic impedance mismatch between the tissue/water (~ 1.5 Mrayls) and the PZT (~ 20 Mrayls to 30 Mrayls). This reduces the efficiency of the transducer due to poor acoustic transmission. One solution is to add an acoustic matching layer between the water and the PZT. Furthermore, so-called piezoelectric composites introduced in the 1970s, often shortened to piezocomposites, tend to display more appropriate properties for some applications and are chosen instead of pure PZT. As the name suggests, a piezocomposite consists of a piezoelectric material, such as PZT, embedded in a piezoelectric inactive material, such as an epoxy or a polymer. 1-3 piezocomposites, which are made of PZT pillars surrounded by an epoxy/polymer, are known to convert acoustic energy to electrical energy and vice versa more efficiently than pure PZT [3]. Another advantage is that, depending on the application, material parameters of the piezocomposite can be changed by varying the PZT volume fraction and dimensions of the PZT pillars. This makes it possible to build composites for a wide range of applications.

1-3 piezocomposites have been studied experimentally and numerically [4, 5]. Numerical investigation is often desired before fabrication to predict the frequency behaviour when the composite is electrically excited by a sinusoidal voltage and oscillates along the thickness direction of the rods. One of the most widely used methods is the Finite Element Method (FEM), which may be used to analyze finite or infinite structures by specifying appropriate boundary conditions. Analytical models also exist, where the composite is described as one homogeneous medium with effective material parameters [3]. These depend on the PZT volume fraction and the material properties of both the PZT and the piezoelectrical inactive material. It can be used as long as the lateral spatial scale of the composite is sufficiently fine compared to all relevant wavelengths of waves propagating in the composite.

When the piezocomposite is electrically and/or mechanically excited, it heats up due to dielectric, mechanical and piezoelectric losses. Its material properties may change depending on the magnitude of the voltage and resulting temperature increase. In ultrasound diagnostics, it is essential that either sufficient cooling is provided or a low enough voltage is applied to prevent the tissue from overheating. The same applies to underwater applications, where severe temperature rises may reduce the capability of the device to transmit/receive ultrasonic waves. Therefore, transducer manufacturers would benefit from accurate predictions of the temperature rise for a given voltage and frequency in order to keep the transducers within a safe temperature range. Such predictions rely on accurate models for the heat generation due to the energy loss mechanisms and for the heat transfer within the piezocomposite, which is mainly limited by relatively low thermal conductivities.

In the first part of this thesis, the heat generation in AC-driven 1-3 composites with fixed material properties and thicknesses but varying PZT volume fractions and lateral square PZT pillar sizes will be investigated using the finite element method over frequency domains including the fundamental thickness resonance and anti-resonance frequency of the composites. Due to limited computational resources, unit cell models are established, described in Section 3.1. In the next section, a quarter-wavelength matching layer with an applied water load will be added to one of the composite models. Finally, the extended model of a composite with its resultant spatial heat generation is imported into a steady-state heat transfer model with appropriate boundary conditions to compute the temperature distribution throughout the entire structure. All simulations will be performed in the FEM software

COMSOL Multiphysics [6].

The theoretical background is presented in Chapter 2. This Chapter is followed by Chapter 3 on aspects of the FEM modeling. Next, Chapter 4 presents the results, before they are discussed in Chapter 5. Finally, conclusions are drawn in Chapter 6.

For tensors/matrices, index notation will sometimes be used. Greek (Roman) indices will range from 1-6 (1-3), unless otherwise stated. A Roman index following a comma means spatial partial derivative. Einstein's summation convention applies for repeated indices unless otherwise stated.

Chapter 2

Theoretical background

This Chapter gives an overview of the theoretical aspects of this thesis. In each Section, a brief outline and motivation will be given before the relevant material is presented.

2.1 Wave propagation in linear elastic materials

This Section 2.1 starts with the symmetry of linear elastic materials. Linear elastic isotropic materials will also be considered as the epoxy of the 1-3 piezocomposites and the matching layer are described as such materials. Then, the elastic wave equation is derived to see how the elastic stiffness for a linear elastic material comes to display in the wave velocities of the waves propagating in such a medium. Furthermore, reflection of pressure waves on material boundaries will be reviewed. This will prove to be very helpful for FEM modeling purposes. In the last Subsection, the basis for attenuation of elastic waves is derived, which will be used extensively in the FEM modeling to incorporate mechanical losses of the epoxy of the 1-3 piezocomposites and the matching layer.

2.1.1 Linear elastic materials

The strain tensor S_{ij} of rank-2 for a solid is defined in terms of the displacement vector ξ_i . It reads [2]

$$S_{ij} = \frac{1}{2}(\xi_{i,j} + \xi_{j,i}), \quad (2.1)$$

reminding the reader that in the subscript notation, Roman indices after a comma amount to spatial partial derivatives. This tensor is readily symmetric:

$$S_{ij} = S_{ji}. \quad (2.2)$$

An elastic material has the ability to return to its initial state after being deformed by external forces [2]. If the material also is linear, Hooke's law applies, which reads

$$T_{ij} = c_{ijkl}S_{kl} \equiv \sum_{k=1}^3 \sum_{l=1}^3 c_{ijkl}S_{kl}, \quad (2.3)$$

where T_{ij} is the stress (rank-2 tensor) and c_{ijkl} is the elastic stiffness (rank-4 tensor). Einstein's summation convention applies for repeated indices as is shown explicitly here. It can be shown that T_{ij} is also symmetric and hence, both of the rank-2 tensors have at most 6 independent coefficients and may be written as 6×1 matrices, that is, column vectors of length 6 [2]. Then, c_{ijkl} can be represented by a 6×6 matrix. Invoking Voigt notation [2], Hooke's law can be rewritten to [2]

$$\vec{T} = \mathbf{c}\vec{S}, \quad (2.4)$$

defining

$$\vec{T} = \begin{bmatrix} T_{11} \\ T_{22} \\ T_{33} \\ T_{23} \\ T_{13} \\ T_{12} \end{bmatrix} \equiv \begin{bmatrix} T_1 \\ T_2 \\ T_3 \\ T_4 \\ T_5 \\ T_6 \end{bmatrix} \quad \text{and} \quad \vec{S} = \begin{bmatrix} S_{11} \\ S_{22} \\ S_{33} \\ 2S_{23} \\ 2S_{13} \\ 2S_{12} \end{bmatrix} \equiv \begin{bmatrix} S_1 \\ S_2 \\ S_3 \\ S_4 \\ S_5 \\ S_6 \end{bmatrix}. \quad (2.5)$$

The elastic compliance matrix \mathbf{s} is defined as the inverse of the elastic stiffness matrix:

$$\mathbf{s} = \mathbf{c}^{-1}. \quad (2.6)$$

Thus, Hooke's law can also be expressed as

$$S_\alpha = s_{\alpha\beta}T_\beta. \quad (2.7)$$

For a linear elastic isotropic material, the elastic stiffness matrix \mathbf{c} has only two dependent variables:

$$\mathbf{c} = \begin{bmatrix} c_{11} & c_{12} & c_{12} & 0 & 0 & 0 \\ c_{12} & c_{11} & c_{12} & 0 & 0 & 0 \\ c_{12} & c_{12} & c_{11} & 0 & 0 & 0 \\ 0 & 0 & 0 & c_{66} & 0 & 0 \\ 0 & 0 & 0 & 0 & c_{66} & 0 \\ 0 & 0 & 0 & 0 & 0 & c_{66} \end{bmatrix}, \quad (2.8)$$

where $c_{66} = (c_{11} - c_{12})/2$.

Consider the stress vector in Eq. (2.5). The first three components correspond to the normal stresses, while the last three give the tangential stresses. The latter are better known as shear stresses. Correspondingly, the first three components of the strain vector relate to normal relative displacements, whereas the last three are shear relative deformations. Furthermore, the non-zero non-diagonal components of the elastic stiffness matrix in Eq. (2.8) act as transverse coupling coefficients. For instance, consider

$$T_1 = c_{11}S_1 + c_{12}(S_2 + S_3). \quad (2.9)$$

Here, the normal stress on a face with normal vector pointing in the 1-direction is not only related to the strain component parallel to the 1-direction, but also to the strains in the other two directions perpendicular to the 1-direction.

2.1.2 The elastic wave equation

Newton's 2nd law gives the equation of motion for an elastic solid. When applied on a medium of uniform mass density ρ and body forces per unit volume f_i , it reads [2]

$$T_{ij,j} + f_i = \rho \frac{\partial^2 \xi_i}{\partial t^2}, \quad (2.10)$$

where the second order partial derivative on the right hand side is with respect to time t . Under the assumption of no volume forces and linear elasticity, the definition of the strain tensor Eq. (2.1) and Hooke's law Eq. (2.3) give

$$c_{ijkl}\xi_{k,jl} = \rho \frac{\partial^2 \xi_i}{\partial t^2}. \quad (2.11)$$

This Equation can be seen as a generalized form of the scalar elastic wave equation for pressure waves propagating in a fluid with sound speed v [2]:

$$\frac{\partial^2 \xi(x, t)}{\partial x^2} = \frac{1}{v^2} \frac{\partial^2 \xi(x \pm vt)}{\partial t^2}, \quad (2.12)$$

whose plane wave solution is

$$\xi(x, t) = \xi_+ e^{i(\omega t + kx)} + \xi_- e^{i(\omega t - kx)}. \quad (2.13)$$

Subscript $+$ denotes backward-propagating wave, $-$ forward-propagating wave. ω is the angular frequency and k is the wavenumber.

Eq. (2.11) implies that the deformation along a direction is a result of propagation of both pressure waves (longitudinal) and shear waves (transverse). For a linear elastic isotropic solid, the respective wave velocities read

$$v_l = \sqrt{\frac{c_{11}}{\rho}} \quad (2.14)$$

and

$$v_s = \sqrt{\frac{c_{66}}{\rho}}. \quad (2.15)$$

2.1.3 One-dimensional propagation of pressure waves in a free medium

Consider one-dimensional propagation of plane waves in a medium of thickness L . In the case of free boundary conditions on both ends, the acoustic pressure p must be zero at these boundaries. As the acoustic wave equation is analogous to the wave equation Eq. (2.12) in terms of displacement, it is straightforward to show that with these boundary conditions, the wave equation implies that

$$\sin k_n L = n\pi \implies \lambda_n = \frac{2L}{n}, n \in \{1, 2, 3, \dots\}, \quad (2.16)$$

where the wavelength λ_n of the n^{th} harmonic was introduced.

2.1.4 Reflections on boundaries between semi-infinite and finite-sized media

Above, propagation in one medium was assumed. Now, consider a plane wave propagating in a semi-infinite medium with density ρ_0 and sound speed v_0 normally incident on a finite-sized medium of thickness L with material parameters ρ_1 and v_1 . At the boundary between the media, the incident wave will be partly reflected back into medium 0 and transmitted into medium 1. Imagine that the transmitted wave is normally incident upon another semi-infinite medium 2 with material parameters ρ_2, v_2 . Define the characteristic acoustic impedance of medium i as $Z_i = \rho_i c_i, i \in \{0, 1, 2\}$. Then, the reflection coefficient R , defined as the ratio of the amplitude of the reflected pressure wave at the second boundary to the amplitude of the incident pressure wave, reads [7]

$$R = \frac{\left(1 - \frac{Z_0}{Z_2}\right) \cos k_1 L + j \left(\frac{Z_1}{Z_2} - \frac{Z_0}{Z_1}\right) \sin k_1 L}{\left(1 + \frac{Z_0}{Z_2}\right) \cos k_1 L + j \left(\frac{Z_1}{Z_2} + \frac{Z_0}{Z_1}\right) \sin k_1 L}. \quad (2.17)$$

For $k_1 L = (n - 1/2)\pi$ and $Z_1 = \sqrt{Z_0 Z_2}$, R vanishes, giving perfect transmission. Meanwhile, for $k_1 L \ll 1$, when the finite-sized medium is very small compared to the wavelength, R simplifies to

$$R \approx \frac{1 - \frac{Z_0}{Z_2} + j \left(\frac{Z_1}{Z_2} - \frac{Z_0}{Z_1}\right) k_1 L}{1 + \frac{Z_0}{Z_2} + j \left(\frac{Z_1}{Z_2} + \frac{Z_0}{Z_1}\right) k_1 L} \approx \frac{1 - \frac{Z_0}{Z_2}}{1 + \frac{Z_0}{Z_2}}. \quad (2.18)$$

This means that the finite-sized medium has a negligible impact on the acoustic transmission into the second semi-infinite medium.

2.1.5 Losses

In an ideal elastic solid, a wave could in principle propagate infinitely far. In real solids however, attenuation of waves occurs, mainly due to absorption and dissipation [8]. The first phenomena involves the conversion to thermal

energy, while dissipation takes place in media with heterogeneities on which the incident wave is scattered.

One way to incorporate losses into the wave equation Eq. (2.12) is to introduce a complex wavenumber with a real part k' and an imaginary part $\alpha > 0$ called the attenuation coefficient [9]:

$$k = k' - i\alpha. \quad (2.19)$$

If one considers pure longitudinal (shear) waves, the displacement $\vec{\xi}$ of the solid will be parallel (normal) to the direction of propagation. For simplicity, consider a plane wave propagating along the 3-direction, i.e. the z -direction. Say that the displacement ξ_3 has a local maximum at $z = z_m$. Then, after propagating one wavelength λ further, the displacement will have a new local maximum, but due to the attenuation coefficient, ξ_3 is reduced by a factor of

$$\frac{\xi_3(z_m + \lambda, t)}{\xi_3(z_m, t)} = \exp(-\alpha\lambda) \equiv \exp(-\pi/Q), \quad (2.20)$$

defining the quality factor Q . Accordingly,

$$Q = \frac{\pi}{\alpha\lambda} = \frac{k'}{2\alpha}. \quad (2.21)$$

The solution Eq. (2.13) inserted into the scalar wave equation Eq. (2.12) yields, with the complex k Eq. (2.19),

$$v = \frac{\omega}{k} = \frac{\omega/k'}{1 + (\frac{\alpha}{k'})^2} \left(1 + i\frac{\alpha}{k'}\right) = \frac{\omega/k'}{1 + (\frac{1}{2Q})^2} \left(1 + i\frac{1}{2Q}\right). \quad (2.22)$$

For $Q \gg 1$, or equivalently $\alpha \ll k'$,

$$v \approx \frac{\omega}{k'} \left(1 + i\frac{1}{2Q}\right) \equiv v' \left(1 + i\frac{v''}{v'}\right), \quad (2.23)$$

introducing the real and imaginary part of the complex velocity for sufficiently high Q . Relating the complex velocity to the complex stiffness

$$c = c' + ic'' = c' \left(1 + \frac{i}{Q_m}\right) \quad (2.24)$$

via Eq. (2.14) (longitudinal) or Eq. (2.15) (shear), one finds that the mechanical quality factor Q_m can be expressed in terms of Q by [9]

$$Q_m = Q - \frac{1}{4Q} \approx Q, \quad (2.25)$$

where the last equality is valid as long as $Q \gg 1$.

2.2 Piezoelectricity

This Subsection starts with an introduction to linear dielectrics. The epoxy of the 1-3 piezocomposites will be electrically described as such a material. The piezoelectrical equations are reviewed along with the material coefficients. Next, the theory behind piezoelectric ceramics is given, along with the symmetry of poled PZTs to express the material coefficient matrices. Then, using Richard Holland's approach [10], the power dissipation density P_d in AC-voltage driven piezoelectrics due to mechanical, dielectric and piezoelectric losses is derived. It will be shown that the power dissipation density can be written as a sum of three terms, one for each energy loss mechanism. The terms related to the mechanical and dielectric losses are also valid for description of the power dissipation density in the piezoelectric inactive materials. This is because the matching layer and the epoxy of the 1-3 piezocomposites are both linear elastic isotropic materials. As the epoxy will also be modeled electrically as a linear dielectric, the dielectric losses applies to it as well. Ultimately, the power dissipation density in the piezocomposite and matching layer amounts to the heat generation that will be imported and used as the heat source in the steady-state heat transfer FEM model.

2.2.1 Linear dielectrics

In contrast to a conductor where charges may flow freely in the material, the charges of the atoms/molecules in a dielectric medium are confined to their nuclei, hence called bound charges [11]. When an external electric field is applied, the charge configuration of the atoms/molecules is shifted so that microscopic dipole moments appear. On a macroscopic scale, the microscopic

contributions averaged over the volume of the solid give rise to a polarization \vec{P} . For linear dielectrics, \vec{P} is proportional to the total electric field \vec{E} , that is, the sum of the external field and the field as a result of polarization. The constant of proportionality is the vacuum permittivity ϵ_0 times the electric susceptibility matrix χ_e :

$$\vec{P} = \epsilon_0 \chi_e \vec{E}. \quad (2.26)$$

Accordingly, the electric displacement \vec{D} in a linear dielectric is [11]

$$\vec{D} = \epsilon_0 \vec{E} + \vec{P} = \epsilon_0 (\mathbf{I}_3 + \chi_e) \vec{E} \equiv \epsilon \vec{E}, \quad (2.27)$$

defining the permittivity matrix ϵ in the last equality. \mathbf{I}_3 is the 3×3 identity matrix. Under the assumptions that no free charges are present in the dielectric and that ϵ is spatially independent, Gauss' law in differential form for a linear dielectric reads [11]

$$D_{i,i} = \epsilon_{ij} E_{j,i} = 0. \quad (2.28)$$

Here, the Einstein summation convention applies and subscript after the comma denotes partial derivative. Moreover, Faraday's law of induction and Ampere's circuit law read [11]

$$\nabla \times \vec{E} = -\frac{\partial \vec{B}}{\partial t} \quad (2.29)$$

and

$$\nabla \times \vec{H} = \frac{\partial \vec{D}}{\partial t} \quad (2.30)$$

for non-conducting media, where \vec{B} is the magnetic field and \vec{H} is the magnetic field strength. The relation between \vec{H} and \vec{B} for a non-magnetic medium is

$$\vec{B} = \mu_0 \vec{H}, \quad (2.31)$$

where μ_0 is the permeability of free space.

2.2.2 The piezoelectric effect

If a solid is electrically polarized due to applied mechanical stresses and is also mechanically deformed under application of an electric field, it is

characterized as a piezoelectric solid [2]. The former phenomenon is called the direct piezoelectric effect while the latter is named the inverse piezoelectric effect.

For a linear piezoelectric material, the piezoelectric effect is manifested through the constitutive Equations Eqs. (2.32) and (2.33):

$$T_\alpha = c_{\alpha\beta}^E S_\beta - e_{i\alpha} E_i, \quad (2.32)$$

$$D_i = e_{i\alpha} S_\alpha + \epsilon_{ij}^S E_j. \quad (2.33)$$

Here, $e_{i\alpha}$ is a 3×6 matrix representation of the piezoelectric coefficient tensor (rank-3). In these Equations, one sees similarities with the Eqs. (2.4) and (2.27). However, there are two more terms which couple the stress to the electric field and the electric displacement field to the strain, respectively. In accordance with the definition of a piezoelectric solid, the coefficients $e_{\alpha i}$ are called piezoelectric coefficients. Moreover, the direct effect appears in Eq. (2.33) and the inverse effect in Eq. (2.32).

The constants of proportionality in Eqs. (2.32) and (2.33) may be expressed as

$$c_{\alpha\beta}^E = \left(\frac{\partial T_\alpha}{\partial S_\beta} \right)_E, \quad (2.34)$$

$$e_{\alpha i} = - \left(\frac{\partial T_\alpha}{\partial E_i} \right)_S = \left(\frac{\partial D_i}{\partial S_\alpha} \right)_E, \quad (2.35)$$

$$\epsilon_{ij}^S = \left(\frac{\partial D_i}{\partial E_j} \right)_S. \quad (2.36)$$

This clarifies the superscript notation.

Since there are four variables (E_i, D_i, S_α and T_α) and there can only be two independent variables for one pair of piezoelectric equations of which one is electrical and the other is mechanical, there exist three other pairs of piezoelectric equations. These are presented in Appendix A along with their respective coefficients and interrelations between these. In Subsection 3.2.6, some of these relations will be needed to convert between material coefficients. Eqs. (2.32) and (2.33) are called the **e**-form of the piezoelectric equations since the piezoelectric coefficient used here is **e**. The other forms are named the **h**-form, **d**-form and **g**-form.

In the next Subsection, an overview of piezoelectric ceramics will be given along with the form of the dielectric, mechanical and piezoelectric property matrices.

2.2.3 Piezoelectric ceramics

Polycrystalline materials consist of crystalline regions that are randomly oriented, thus macroscopically giving zero polarization [12]. If the material is ferroelectric, it will have a spontaneous polarization in each of these domains for temperatures below the Curie temperature. Applying a sufficiently strong electric field may change the orientation of the domains so that a non-zero macroscopic polarization is achieved. A ferroelectric material with a strong coercive force will be able to keep a remnant polarization even when the strong electric field, known as a polarization field or bias, is turned off [1]. Still, the temperature has to be below the Curie temperature - else, the solid may transition into a paraelectric state, meaning that the spontaneous polarization vanishes along with the the remnant polarization.

At temperatures close to the Curie temperature, the ferroelectric material may be poled through the application of a bias. It is known that poled polycrystalline ferroelectric materials display the same crystal symmetry as piezoelectrics [1]. In particular, the ferroelectric materials BaTiO_3 (barium titanate) and $\text{Pb}[\text{Zr}_x\text{Ti}_{1-x}]\text{O}_3$, $0 \leq x \leq 1$ (lead zirconate titanate, or PZT) have the symmetry of the crystal group $C_{6v} = C_\infty$ when poled. As both also have the properties of a ceramic, they are called piezoelectric ceramics, or just piezoceramics.

The crystal group C_∞ contains crystals that are dihexagonal pyramidal, meaning that these crystals have a 6-fold rotational axis and two perpendicular mirror planes [13]. The poling direction is chosen to be in the 3-direction by convention. It should also be mentioned that this symmetry implies transverse isotropy with respect to the poling direction, the 3-direction. Then, the representation of the piezoelectric, permittivity and elastic compliance tensor in matrix form for piezoceramics poled in the 3-direction read

$$\mathbf{d} = \begin{bmatrix} 0 & 0 & 0 & 0 & d_{15} & 0 \\ 0 & 0 & 0 & d_{15} & 0 & 0 \\ d_{31} & d_{31} & d_{33} & 0 & 0 & 0 \end{bmatrix}, \quad (2.37)$$

$$\boldsymbol{\epsilon} = \begin{bmatrix} \epsilon_{11} & 0 & 0 \\ 0 & \epsilon_{11} & 0 \\ 0 & 0 & \epsilon_{33} \end{bmatrix} = \boldsymbol{\beta}^{-1} \quad (2.38)$$

and

$$\boldsymbol{s} = \begin{bmatrix} s_{11} & s_{12} & s_{13} & 0 & 0 & 0 \\ s_{12} & s_{11} & s_{13} & 0 & 0 & 0 \\ s_{13} & s_{13} & s_{33} & 0 & 0 & 0 \\ 0 & 0 & 0 & s_{44} & 0 & 0 \\ 0 & 0 & 0 & 0 & s_{44} & 0 \\ 0 & 0 & 0 & 0 & 0 & s_{66} \end{bmatrix} = \boldsymbol{c}^{-1}, \quad (2.39)$$

respectively. Here, the inverse permittivity, also known as the impermittivity, $\boldsymbol{\beta}$ was defined, while \boldsymbol{c} is recognized as the stiffness matrix. Also note that $s_{66} = 2(s_{11} - s_{12})$. In other words, there are 3 independent piezoelectric coefficients, 2 independent electric coefficients and 5 independent mechanical coefficients, resulting in 10 independent material parameters in total.

2.2.4 Power dissipation density

When considering the energy balance equation for a piezoelectric, the instantaneous power per unit volume \mathcal{P} can be shown to depend on five terms [2],[10]:

$$\mathcal{P} = \rho \frac{\partial^2 \vec{\xi}}{\partial t^2} \cdot \frac{\partial \vec{\xi}}{\partial t} + \boldsymbol{T} : \frac{\partial \boldsymbol{S}}{\partial t} + \vec{E} \cdot \frac{\partial \vec{D}}{\partial t} + \nabla \cdot \left(-\boldsymbol{T} \cdot \frac{\partial \vec{\xi}}{\partial t} + \vec{E} \times \vec{H} \right). \quad (2.40)$$

Colon means double contraction. The first term is the time derivative of the kinetic energy per unit volume, while the second and third terms contribute to the mechanical potential energy and electric potential energy per unit volume stored in the system. The expression in the brackets is the most important for this discussion. It is identified as the instantaneous Poynting vector $\vec{\Sigma}$, which gives the flow of energy per surface area per unit time:

$$\vec{\Sigma} = -\boldsymbol{T} \cdot \frac{\partial \vec{\xi}}{\partial t} + \vec{E} \times \vec{H} = -\boldsymbol{T} \cdot \vec{u} + \vec{E} \times \vec{H}, \quad (2.41)$$

rewriting the partial derivative of the displacement with respect to time as the particle velocity \vec{u} in the last equality. From now on, complex variables

will be used and harmonic time dependence $\exp(j\omega t)$ with angular frequency ω is assumed for all relevant physical quantities. Then, the complex instantaneous Poynting vector, for simplicity referred to as the Poynting vector later, reads

$$\vec{\Sigma} = \frac{1}{2} \left(\vec{E} \times \vec{H}^* - j\omega \mathbf{T} \cdot \vec{\xi}^* \right). \quad (2.42)$$

The real part of the Poynting vector gives the time averaged energy flow per surface area per unit time. Taking the negative divergence of this yields the power dissipation density P_d :

$$P_d = -\frac{1}{2} \operatorname{Re} \left\{ \nabla \cdot \left(\vec{E} \times \vec{H}^* \right) - j\omega \vec{\xi}^* \cdot (\nabla \cdot \mathbf{T}) - j\omega \mathbf{T} : (\nabla \cdot \vec{\xi}^*) \right\}. \quad (2.43)$$

In the following, Holland's approach [10] will be used to express the power dissipation density first in terms of the electric field, electric displacement field, stress tensor and strain tensor and then in terms of the electric field, strain and material coefficients. The former expression will be convenient in the finite element analyses while the latter shows how the imaginary parts of the material coefficients contribute to the power dissipation density in a piezoelectric.

First, Holland uses the vector identity

$$\nabla \cdot (\vec{E} \times \vec{H}^*) = \vec{H}^* \cdot (\nabla \times \vec{E}) - \vec{E} \cdot (\nabla \times \vec{H}^*) \quad (2.44)$$

to rewrite the power dissipation density Eq. (2.43) in terms of the curl of \vec{E} and the curl of \vec{H} . He then applies Faraday's law of induction Eq. (2.29) and Ampere's circuit law Eq. (2.30) to Eq. (2.44) to exploit the assumed time harmonic dependence of \vec{B} and \vec{D} . As the double contraction of a symmetric tensor with an antisymmetric tensor is zero, only the symmetric part of the gradient of $\vec{\xi}^*$ contributes to the last term in Eq. (2.43) and this is the strain tensor \mathbf{S} . For the divergence of \mathbf{T} , Newton's second law Eq. (2.10) with time harmonic dependence is used. Following these steps and substituting \vec{H} by \vec{B} using Eq. (2.31), Holland's equation for the power dissipation density reduces to

$$P_d = \frac{1}{2} \omega \operatorname{Im} \left\{ \vec{E} \cdot \vec{D}^* + \mathbf{T} : \mathbf{S}^* \right\}. \quad (2.45)$$

This Equation integrated over the volume of the piezoelectric yields the power dissipation. As explained in the beginning of Section 2.2, this Equation will

be used to compute the power dissipation density in the epoxy, PZT and matching layer in the FEM simulations.

Now, introducing mechanical, piezoelectric and dielectric losses by writing the material coefficient in complex form as

$$\mathbf{s}^E = \mathbf{s}^{E'} - j\mathbf{s}^{E''} \quad (2.46)$$

$$\mathbf{d} = \mathbf{d}' - j\mathbf{d}'' \quad (2.47)$$

$$\boldsymbol{\epsilon}^T = \boldsymbol{\epsilon}^{T'} - j\boldsymbol{\epsilon}^{T''}, \quad (2.48)$$

the \mathbf{d} -form of the piezoelectric equations Eqs. (A.3) and (A.4) used on Eq. (2.45) imply that

$$P_d = \frac{1}{2}\omega \operatorname{Im}\{E_i d_{i\alpha}^* T_\alpha^* + E_i \epsilon_{ij}^{T*} E_j^* + T_\alpha s_{\alpha\beta}^{E*} T_\beta^* + E_i^* d_{i\alpha} T_\alpha\}, \quad (2.49)$$

using Voigt notation for the stress tensor \mathbf{T} . Next, Holland conveniently writes the previous Equation in matrix form by first defining the column vector \vec{F} of length 9,

$$\vec{F} = \begin{bmatrix} \vec{T} \\ \vec{E} \end{bmatrix} \quad (2.50)$$

and then the 9×9 symmetric matrix \mathbf{M} composed of the material coefficient matrices:

$$\mathbf{M} = \begin{bmatrix} \mathbf{s}^E & \mathbf{d} \\ \mathbf{d}^t & \boldsymbol{\epsilon}^T \end{bmatrix}, \quad (2.51)$$

\mathbf{d}^t denoting the transpose of \mathbf{d} . This makes it possible to express the power dissipation density compactly as

$$P_d = \frac{1}{2}\omega \operatorname{Im}\{\vec{F}^t \mathbf{M}^* \vec{F}^*\}. \quad (2.52)$$

\vec{F}^t is the transpose of \vec{F} . Now, let θ_{pq} be the phase angle between the vectors F_p and F_q , p, q ranging from 1 to 9. Then, by Euler's formula,

$$F_p F_q = |F_p| |F_q| (\cos \theta_{pq} + j \sin \theta_{pq}), \quad (2.53)$$

no summation over repeated indices. If one uses the same complex notation for M_{pq} as for the material coefficients,

$$M_{pq} = M'_{pq} - jM''_{pq} \quad (2.54)$$

and P_d simplifies to

$$\begin{aligned}
P_d &= \frac{1}{2}\omega \sum_{p,q} |F_p||F_q|(M''_{pq} \cos \theta_{pq} + M'_{pq} \sin \theta_{pq}) \\
&= \frac{1}{2}\omega \sum_{p,q} |F_p||F_q|M''_{pq} \cos \theta_{pq}, \tag{2.55}
\end{aligned}$$

as $\theta_{pq} = -\theta_{qp}$.

Holland concludes that the complex part of \mathbf{s}^E gives a mechanical power loss, the complex part of $\boldsymbol{\epsilon}^T$ gives a an electrical power loss and the complex part of \mathbf{d} gives a power loss depending on the electric field and the mechanical stress. This can be seen more explicitly by rewriting the previous Equation using the definition of M_{pq} Eq. (2.51):

$$\begin{aligned}
P_d &= \frac{1}{2}\omega \sum_{\alpha,\beta} |T_\alpha||T_\beta|s_{\alpha\beta}^{E''} \cos \theta_{\alpha\beta} \\
&\quad + \frac{1}{2}\omega \sum_{i,j} |E_i||E_j|\epsilon_{ij}^{T''} \cos \theta_{ij} \\
&\quad + \omega \sum_{i,\alpha} |E_i||T_\alpha|d''_{i\alpha} \cos \theta_{i\alpha}. \tag{2.56}
\end{aligned}$$

In the last term on the right hand side, the fact that $M_{pq} = M_{qp}$ was used so that the factor of 1/2 vanishes.

2.2.5 Losses in dielectrics and piezoelectrics

In the previous Subsection, it was shown that complex material parameters Eqs. (2.46)-(2.48), in this case \mathbf{s}^E , \mathbf{d} and $\boldsymbol{\epsilon}^T$, give rise to power dissipation in piezoelectrics. In this short Subsection, the physical loss mechanisms will be briefly discussed and alternative loss formulations will be given. As the complex elastic compliance relates to the complex wavenumber presented in Subsection 2.1.5 via the elastic wave equation Eq. (2.11), the mechanical energy loss mechanism has already been explained, so only the electric and piezoelectric loss mechanisms will be considered here.

For a non-ideal dielectric, the response of the polarization to the external electric field is not instantaneous. In other words, there is a phase difference

between the polarization and the electric field. This is denoted by δ_ϵ and is also known as the dielectric loss angle or dielectric loss factor. Along the direction of the external field, the following relationship holds for the complex permittivity:

$$\tan(\delta_\epsilon) = \frac{\epsilon^{T''}}{\epsilon^{T'}}. \quad (2.57)$$

In piezoelectrics, a similar phase difference is observed between the induced electric displacement and applied mechanical stress (direct effect) and between the induced mechanical stress and applied electric field (inverse effect) [14]. Thus, the piezoelectric loss factor reads

$$\tan(\delta_d) = \frac{d''}{d'}. \quad (2.58)$$

2.3 1-3 piezocomposites

In the previous Section, the energy loss mechanisms in the piezoelectric inactive (epoxy) and the active material (PZT) of the 1-3 piezocomposites were given. Now, the structure itself will be presented along with its relevant resonances. The use of 1-3 piezocomposites for underwater ultrasonic applications was motivated in Chapter 1. Subsection 2.3.3, deriving the material parameters of the effective medium model [3], will be especially important with regards to determining the appropriate acoustic properties of the matching layer and provides verification of the fundamental thickness resonances obtained in the FEM simulations. The last Subsection presents an equivalent but simpler expression for the power dissipation obtained by Holland's approach [10] in the case of an AC-driven 1-3 piezocomposite operating in vacuum.

2.3.1 Materials and composition

1-3 piezoelectric composites, often shorted to 1-3 piezocomposites, consist of a piezoelectric material, usually PZT, and an epoxy, mostly piezoelectric inactive. The 1-3 relates to the connectivity: The first digit, 1, means that the piezoelectric material is connected along one direction only, which will

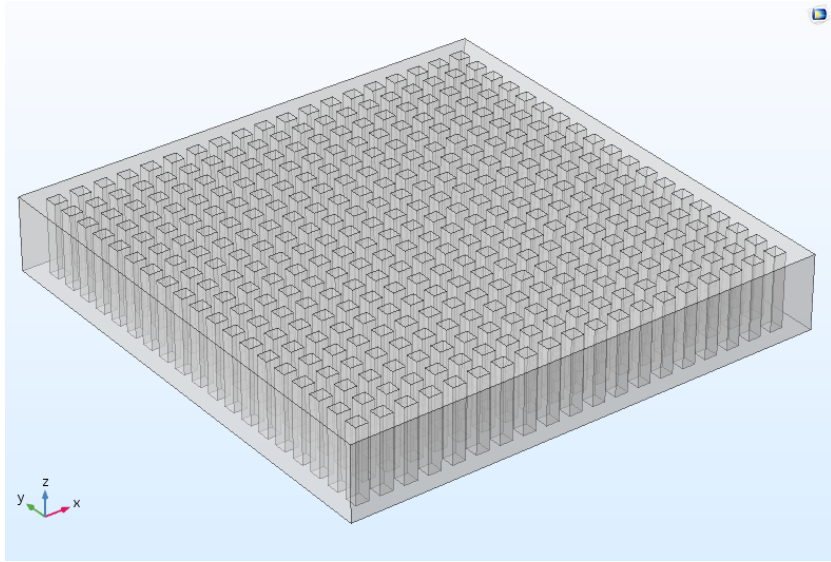


Fig. 2.1: Model of a 1-3 composite with 19×19 square pillars and equal periodicity in the lateral directions (x and y -axis). The thickness direction is along the z -axis.

be termed the thickness direction. The second number, 3, indicates that the epoxy is connected in all three directions. The directions along the coordinate axes normal to the thickness direction are called lateral directions.

A model of such a 1-3 composite is shown in Fig. 2.1. It can be seen that the 1-3 connectivity implies rod or pillar like shapes for the piezoelectric material, in this case with square lateral cross sections. Depending on the application, 1-3 composites may consist of pillars displaying other geometrical shapes and appearing in semi-periodic patterns. For this discussion, assume the same periodicity along both lateral directions. Also, let the lateral cross section of the rods be square and the rods have the same thickness as the surrounding epoxy. Fig. 2.1 is applicable to this situation.

In Fig. 2.2, a portion of the same composite is viewed from above and two lateral measures are given: The rod size w_r and the rod spacing Δw_r .

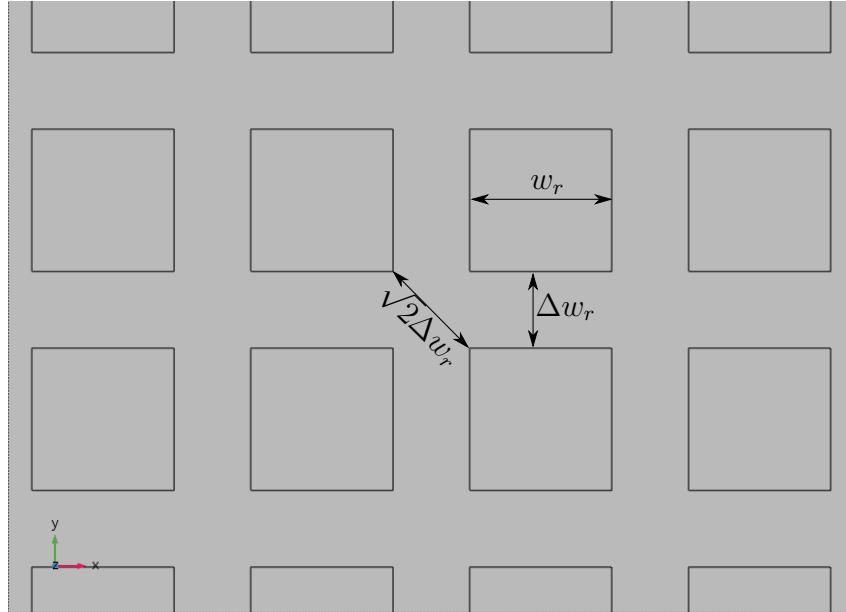


Fig. 2.2: A portion of a 1-3 composite in Fig. 2.1 seen from above. The square PZT rod size w_r and rod spacing Δw_r (epoxy) are shown, along with the diagonal rod spacing of $\sqrt{2}\Delta w_r$.

2.3.2 Resonances

To generate ultrasound, the 1-3 piezocomposite is set in motion by exciting the PZT electrically, utilizing the inverse piezoelectric effect. In the case of thickness oscillations, electrodes of a conductive metal are mounted onto the entire top and bottom surface to which a uniform sinusoidal voltage with angular frequency ω is applied. Depending on the frequency of the applied voltage, different vibrational modes are excited. The fundamental thickness resonance frequency f_r of the composite (with electrodes) is given by the frequency at which the first minimum in the absolute value of the electrical impedance $|Z| = |Z(\omega)|$ measured over the electrodes occurs [15]. The corresponding fundamental anti-resonance frequency f_a is found at the frequency of the first maximum of the absolute value of $|Z(\omega)|$ [15].

Other important frequencies are the series f_s and parallel f_p resonance frequencies. These frequencies can be found in two ways. By the definition, f_s (f_p) occurs at the frequency of the first maximum in conductance $G = G(\omega)$

(resistance $R = R(\omega)$) [15]. For a 1-3 composite, however, an estimate of these frequencies can be computed by assuming the composite to behave as an effective medium for which the effective longitudinal velocities are given in terms of the material parameters and volume fractions of the PZT and epoxy. This model will be presented in the next Subsection - for now, the expressions will just be given. The series resonance frequency can be estimated by

$$f_s \approx \frac{\bar{v}_l^E}{2t_c}, \quad (2.59)$$

where the effective longitudinal wave velocity of the composite \bar{v}_l^E at constant electric field was introduced, along with the thickness of the composite t_c . Constant electric field can be achieved by short-circuiting the electrodes. An approximation of the parallel resonance frequency is

$$f_p \approx \frac{\bar{v}_l^D}{2t_c} > f_s. \quad (2.60)$$

As before, \bar{v}_l^D denotes the effective longitudinal wave velocity in the composite, this time, however, evaluated at constant electric displacement. This condition is met for an open circuit, that is, keeping the charge on the electrodes constant. In lossy composites, the following holds in general [15]:

$$f_r > f_s, \quad (2.61)$$

$$f_a < f_p. \quad (2.62)$$

For applications where the composite is used in thickness mode, the rod spacing Δw_r , rod size w_r and ceramic aspect ratio AR, the latter given as w_r/t_c , have to be chosen carefully. If not, lateral resonance modes may develop within the frequency operating range of the composite, reducing its efficiency. In [4], the resonance frequencies of two types of inter-pillar lateral modes in the piezoelectric inactive medium (epoxy) have been related to the rod spacing. The first kind is half-wave standing wave patterns in between the faces of adjacent rods, while the second type is half-wave standing wave patterns developing along the extension of the diagonal between neighbouring rods, see Fig. 2.2. In both cases, the fundamental resonance frequencies were found to agree well with that of half-wave resonators for a wide range of volume fractions. Since the diagonal pillar spacing is a factor $\sqrt{2}$ longer than the lateral rod spacing, the fundamental diagonal resonance f_{t1} is expected

to occur at a frequency given by the fundamental lateral resonance f_{t2} times $1/\sqrt{2}$. The resonances were found to be well-defined by the rod spacing and shear wave velocity in the epoxy v_s through the expressions

$$f_{t2} = \sqrt{2}f_{t1} = \frac{v_s}{2\Delta w_r} \quad (2.63)$$

as long as π/t_c was sufficiently small.

2.3.3 The effective medium model for thickness-model oscillations in 1-3 piezocomposites

The derivation of the effective medium model [3] given here will be following the same procedures as presented there. Though, as the goal is to obtain effective material properties for determination of the effective resonance frequencies \bar{f}_s and \bar{f}_p only, some of the derivations presented there are conveniently left out. Throughout the derivation, no losses are incorporated, meaning that the material coefficients are real.

A few initial remarks are necessary for the reader. As in [3], the \mathbf{e} -form Eqs. (2.32) and (2.33) of the piezoelectric equations will be used. This amounts to \vec{T} and \vec{D} as independent variables. The piezoelectric medium will be described with the C_∞ -symmetry as defined in Subsection 2.2.3 and the epoxy will be a linear elastic isotropic material with stiffness \mathbf{c} as given by Eq. (2.8). Electrically, the epoxy will be considered as a linear dielectric medium with homogeneous and isotropic permittivity ϵ_{11} . This corresponds to a diagonal permittivity matrix with ϵ_{11} . Linear dielectrics were described in Subsection 2.2.1.

For each material, there are initially 6 equations for the components of the stress \vec{T} and 3 equations for the electric displacement \vec{D} . For clarity, they

will be given here. First for the epoxy:

$$T_1 = c_{11}S_1 + c_{12}S_2 + c_{12}S_3 \quad (2.64a)$$

$$T_2 = c_{12}S_1 + c_{11}S_2 + c_{12}S_3 \quad (2.64b)$$

$$T_3 = c_{12}S_1 + c_{12}S_2 + c_{11}S_3 \quad (2.64c)$$

$$T_4 = c_{44}S_4 \quad (2.64d)$$

$$T_5 = c_{44}S_5 \quad (2.64e)$$

$$T_6 = c_{44}S_6 \quad (2.64f)$$

$$D_1 = \epsilon_{11}E_1 \quad (2.64g)$$

$$D_2 = \epsilon_{11}E_2 \quad (2.64h)$$

$$D_3 = \epsilon_{11}E_3 \quad (2.64i)$$

and then for the ceramic:

$$T_1 = c_{11}^E S_1 + c_{12}^E S_2 + c_{13}^E S_3 - e_{31} E_3 \quad (2.65a)$$

$$T_2 = c_{12}^E S_1 + c_{11}^E S_2 + c_{13}^E S_3 - e_{31} E_3 \quad (2.65b)$$

$$T_3 = c_{13}^E S_1 + c_{13}^E S_2 + c_{33}^E S_3 - e_{33} E_3 \quad (2.65c)$$

$$T_4 = c_{44}^E S_4 - e_{15} E_2 \quad (2.65d)$$

$$T_5 = c_{44}^E S_5 - e_{15} E_1 \quad (2.65e)$$

$$T_6 = c_{66}^E S_6 \quad (2.65f)$$

$$D_1 = e_{15} S_5 + \epsilon_{11}^S E_1 \quad (2.65g)$$

$$D_2 = e_{15} S_4 + \epsilon_{11}^S E_2 \quad (2.65h)$$

$$D_3 = e_{31} S_1 + e_{31} S_2 + e_{33} S_3 + \epsilon_{33}^S E_3. \quad (2.65i)$$

The first approximation introduced in the effective medium model is that the strain \vec{S} and electric field \vec{E} are independent of the transverse coordinates x and y . As is pointed out, this does not hold in general as can be seen in finite element analysis and the assumption is made to describe these variables in an average sense. Superscript p (c) will be used for physical quantities in the epoxy (ceramic) phase. However, the quantities \mathbf{c} , $\boldsymbol{\epsilon}$ and $\boldsymbol{\beta}$ in the piezoelectric will be written in terms of the conventional superscript notation as introduced in Subsection 2.2.2.

Second, symmetry in the x - y plane is assumed. As both materials are transversely isotropic with respect to the thickness direction z , this seems fair.

This implies that only one of the equations for the lateral stresses is needed in each material as the stress in the x -direction is equal to the stress in the y -direction. Further, the transverse electric field components are assumed to be zero, which should be valid if the electrodes are equipotentials. Moreover, the shear components of the stress are disregarded in both materials as only thickness oscillations will be considered. The relevant equations now read

$$T_1^p = (c_{11} + c_{12})S_1^p + c_{12}S_3^p, \quad (2.66a)$$

$$T_3^p = 2c_{12}S_1^p + c_{11}S_3^p, \quad (2.66b)$$

$$D_3^p = \epsilon_{11}E_3^p \quad (2.66c)$$

for the epoxy and

$$T_1^c = (c_{11}^E + c_{12}^E)S_1^c + c_{13}^E S_3^c - e_{31}E_3^c, \quad (2.67a)$$

$$T_3^c = 2c_{13}^E S_1^c + c_{33}^E S_3^c - e_{33}E_3^c, \quad (2.67b)$$

$$D_3^c = 2e_{31}S_1^c + e_{33}S_3^c + \epsilon_{33}^S E_3^c \quad (2.67c)$$

for the piezoelectric. The irrelevant equations for the shear stresses (3 in each material) have been left out together with one of the equations equation for the lateral stresses (1). The electric displacement in the transverse plane (2) vanishes in the epoxy and is disregarded in the ceramic. Thus, 9 initial equations in each material have been narrowed down to 3 in each phase.

The third approximation introduces uniform thickness oscillations, imposing equal vertical strains over the composite materials:

$$S_3^p = S_3^c = \bar{S}_3(z). \quad (2.68)$$

This is also known as the iso-strain condition. As introduced earlier in Subsection 2.3.2, the bar will be used to denote effective quantities. If the lateral resonance modes occur at much higher frequencies, this approximation is reasonable. They do so if the epoxy width Δw_r introduced in Fig. 2.2 is small enough compared to all relevant wavelengths of waves propagating in the epoxy. As the shear wave velocity is usually the lowest velocity, the shortest wavelength of waves in the epoxy is given by the ratio of the shear wave velocity to the maximum frequency.

The electrodes are considered to extend over the entire upper and lower surface of the composite and amount to equipotentials. Therefore, the electric

fields is assumed to be the same in both materials along the thickness direction:

$$E_3^{\text{p}} = E_3^{\text{c}} = \bar{E}_3(z). \quad (2.69)$$

The next approximation covers two aspects. First, the lateral stresses are assumed to be equal in both materials. Second, one expects the composite as a whole to be laterally clamped, meaning that the lateral strain in the ceramic must be compensated by a complimentary strain in the epoxy. In terms of the ceramic (epoxy) volume fraction ν ($\tilde{\nu} = 1 - \nu$) of the piezocomposite,

$$T_1^{\text{p}} = T_1^{\text{c}} = \bar{T}_1(z) \quad (2.70)$$

and

$$\bar{S}_1(z) = \tilde{\nu}S_1^{\text{p}}(z) + \nu S_1^{\text{c}} = 0. \quad (2.71)$$

Rewriting the lateral strains S_1^{c} and S_1^{p} as functions of the vertical strain and electric field in both materials yields

$$S_1^{\text{c}} = \tilde{\nu} \frac{-(c_{13}^E - c_{12})\bar{S}_3 + e_{31}\bar{E}_3}{\nu(c_{11} + c_{12}) + \tilde{\nu}(c_{11}^E + c_{12}^E)} \quad (2.72)$$

and

$$S_1^{\text{p}} = \nu \frac{(c_{13}^E - c_{12})\bar{S}_3 - e_{31}\bar{E}_3}{\nu(c_{11} + c_{12}) + \tilde{\nu}(c_{11}^E + c_{12}^E)}. \quad (2.73)$$

This makes it possible to eliminate S_1^{c} and S_1^{p} so that

$$\bar{T}_1(z) = c_{13}^E \bar{S}_3 - \bar{e}_{31} \bar{E}_3, \quad (2.74)$$

with

$$\bar{c}_{13}^E = \frac{\nu c_{13}^E (c_{11} + c_{12}) + \tilde{\nu} c_{12} (c_{11}^E + c_{12}^E)}{\nu(c_{11} + c_{12}) + \tilde{\nu}(c_{11}^E + c_{12}^E)} \quad (2.75)$$

and

$$\bar{e}_{31} = \frac{\nu e_{31} (c_{11} + c_{12})}{\nu(c_{11} + c_{12}) + \tilde{\nu}(c_{11}^E + c_{12}^E)}. \quad (2.76)$$

The stresses and electric displacements in the z -direction become

$$T_3^{\text{p}} = \left[c_{11} + \frac{2\nu c_{12} (c_{13}^E - c_{12})}{\nu(c_{11} + c_{12}) + \tilde{\nu}(c_{11}^E + c_{12}^E)} \right] \bar{S}_3 - \left[\frac{2\nu e_{31} c_{12}}{\nu(c_{11} + c_{12}) + \tilde{\nu}(c_{11}^E + c_{12}^E)} \right] \bar{E}_3 \quad (2.77)$$

$$D_3^p = \epsilon_{11} \bar{E}_3 \quad (2.78)$$

for the epoxy and

$$T_3^c = \left[c_{33}^E - \frac{2\tilde{\nu}c_{13}^E(c_{13}^E - c_{12})}{\nu(c_{11} + c_{12}) + \tilde{\nu}(c_{11}^E + c_{12}^E)} \right] \bar{S}_3 - \left[e_{33} - \frac{2\tilde{\nu}e_{31}c_{13}^E}{\nu(c_{11} + c_{12}) + \tilde{\nu}(c_{11}^E + c_{12}^E)} \right] \bar{E}_3 \quad (2.79)$$

$$D_3^c = \left[e_{33} - \frac{2\tilde{\nu}e_{31}(c_{13}^E - c_{12})}{\nu(c_{11} + c_{12}) + \tilde{\nu}(c_{11}^E + c_{12}^E)} \right] \bar{S}_3 + \left[\epsilon_{33}^S + \frac{2\tilde{\nu}(e_{31})^2}{\nu(c_{11} + c_{12}) + \tilde{\nu}(c_{11}^E + c_{12}^E)} \right] \bar{E}_3. \quad (2.80)$$

for the ceramic.

To obtain the effective medium parameters, one last assumption is needed. Along the thickness direction, the effective total stress \bar{T}_3 and displacement \bar{D}_3 are acquired by averaging the stresses and displacements with respect to the volume fractions:

$$\bar{T}_3(z) = \nu T_3^c(z) + \tilde{\nu} T_3^p(z) \quad (2.81)$$

$$\bar{D}_3(z) = \nu D_3^c(z) + \tilde{\nu} D_3^p(z). \quad (2.82)$$

The effective material properties read

$$\bar{c}_{33}^E = \nu \left[c_{33}^E - \frac{2\tilde{\nu}(c_{13}^E - c_{12})^2}{\nu(c_{11} + c_{12}) + \tilde{\nu}(c_{11}^E + c_{12}^E)} \right] + \tilde{\nu}c_{11} \quad (2.83)$$

$$\bar{e}_{33} = \nu \left[e_{33} - \frac{2\tilde{\nu}e_{31}(c_{13}^E - c_{12})}{\nu(c_{11} + c_{12}) + \tilde{\nu}(c_{11}^E + c_{12}^E)} \right] \quad (2.84)$$

$$\bar{\epsilon}_{33}^S = \nu \left[\epsilon_{33}^S + \frac{2\tilde{\nu}(e_{31})^2}{\nu(c_{11} + c_{12}) + \tilde{\nu}(c_{11}^E + c_{12}^E)} \right] + \tilde{\nu}\epsilon_{11}. \quad (2.85)$$

The final constitutive equations for the effective medium oscillating in the thickness direction become

$$\bar{T}_3(z) = \bar{c}_{33}^E \bar{S}_3 - \bar{e}_{33} \bar{E}_3 \quad (2.86)$$

$$\bar{D}_3(z) = \bar{e}_{33}^E \bar{S}_3 - \bar{\epsilon}_{33}^S \bar{E}_3. \quad (2.87)$$

To check the effective material properties at the extremities, consider first $\nu = 1$, which amounts to a piezoelectric plate:

$$\left(\bar{c}_{33}^E\right)_{\nu=1} = c_{33}^E \quad (2.88)$$

$$\left(\bar{e}_{33}\right)_{\nu=1} = e_{33} \quad (2.89)$$

$$\left(\bar{\epsilon}_{33}^S\right)_{\nu=1} = \epsilon_{33}^S. \quad (2.90)$$

Then, let $\nu = 0$. This yields an epoxy slab:

$$\left(\bar{c}_{33}^E\right)_{\nu=0} = c_{11} = c_{33} \quad (2.91)$$

$$\left(\bar{e}_{33}\right)_{\nu=0} = 0 \quad (2.92)$$

$$\left(\bar{\epsilon}_{33}^S\right)_{\nu=0} = \epsilon_{11} = \epsilon_{33}. \quad (2.93)$$

Introducing the effective density

$$\bar{\rho} = \nu\rho^c + \tilde{\nu}\rho^p, \quad (2.94)$$

the effective specific impedance is \bar{Z} :

$$\bar{Z} = \sqrt{\bar{c}_{33}^D \bar{\rho}}, \quad (2.95)$$

the effective stiffness under short-circuit conditions \bar{c}_{33}^D given by

$$\bar{c}_{33}^D = \bar{c}_{33}^E + (\bar{e}_{33})^2 / \bar{\epsilon}^S \quad (2.96)$$

by Eqs. (A.10) and (A.11). The effective longitudinal velocity under open-circuit conditions \bar{v}_1^D reads

$$\bar{v}_1^D = \sqrt{\bar{c}_{33}^D / \bar{\rho}}, \quad (2.97)$$

while under short-circuit conditions, it reads

$$\bar{v}_1^E = \sqrt{\bar{c}_{33}^E / \bar{\rho}}. \quad (2.98)$$

Finally, this gives the expressions for the effective fundamental series \bar{f}_s and effective fundamental parallel \bar{f}_p resonance frequency as given in Subsection 2.3.2:

$$\bar{f}_p = \frac{\bar{v}_l^D}{2t_c} \quad (2.99)$$

and

$$\bar{f}_s = \frac{\bar{v}_l^E}{2t_c}, \quad (2.100)$$

reminding the reader that t_c is the thickness of the composite.

2.3.4 Ohm's law and the Joule heating law

Ohm's law states that the voltage drop V over an electrical conductor of resistance R is equal to the product of the current I through the resistor and R [11]:

$$V = RI. \quad (2.101)$$

As current flows through the conductive material, some of the electric energy of the current is generated into heat. For a resistive element, the power loss P due to heating is given by the product of the current and the voltage drop [11]:

$$P = VI = RI^2. \quad (2.102)$$

In the last equality, Ohm's law Eq. (2.101) was used. Eq. (2.102) is known as the Joule heating law and the phenomenon is called Joule heating. Assuming a sinusoidal varying voltage $V = V_0 \exp(j\omega t)$ and using complex notation, the Joule heating law may be rewritten as

$$P = \frac{1}{2} \operatorname{Re}\{UI^*\}, \quad (2.103)$$

I^* denoting the complex conjugate of the current. Note that this P is equal to the time-averaged power dissipation, which is generally frequency dependent, $P = P(\omega)$. Ohm's law reads

$$U = IZ = I(R + jX), \quad (2.104)$$

where Z is the electrical impedance and X is the reactance. Writing the admittance $Y = Z^{-1} = G + jB$ with conductance G and susceptance B , it

is easy to show that

$$P = \frac{1}{2}|V_0|^2 G, \quad (2.105)$$

using Ohm's law Eq. (2.104) to rewrite the current in terms of the voltage and impedance.

This applies to currents due to free charges as well as currents due to bound charges. Thus, for an AC-voltage driven 1-3 piezocomposite in vacuum, the electrical power input to the composite given by Eq. (2.105) is equivalent with the power dissipation density P_d in Eq. (2.45) integrated over the volume of the composite. In the Discussion, this will be checked explicitly for one of the composites in vacuum. Although Eq. (2.45) was deduced for a piezoelectric, it applies equally well for a composite as long as the epoxy/polymer in the composite is a linear elastic material. The piezoelectric inactive material of the composite will not give any piezoelectric loss contribution, though, only mechanical and dielectric loss contributions (the epoxy will be modeled electrically as a linear dielectric).

2.4 Heat transfer

This Section covers the background material for steady-state heat transfer. Boundary conditions for radiation and convection will be discussed in Section 3.4.

2.4.1 Fourier's law

In a medium with a non-uniform temperature distribution, heat will flow from the warmer to the colder areas to relax the system into thermal equilibrium. Fourier's law gives the relation between the heat flux \vec{q} flowing through a material with thermal conductivity k and the temperature gradient ∇T . It reads [13]

$$\vec{q} = -k\nabla T. \quad (2.106)$$

2.4.2 The heat equation

The general form of the heat equation is

$$c_p \rho \frac{\partial T}{\partial t} = \nabla \cdot (k \nabla T) + Q_s, \quad (2.107)$$

where c_p and ρ denote the specific heat capacity at constant pressure and mass density, respectively. The first term on the right hand side is the divergence of the negative heat flux as given by Fourier's law Eq. (2.106). The second term $Q_s = Q_s(\vec{r}, t)$ is a source or/and sink term which incorporates phenomena such as heat generation, radiation and convection into the equation. \vec{r} is the position vector and t is the time variable. Eq. (2.107) is solved for $T = T(\vec{r}, t)$ to obtain the temperature distribution.

For steady-state heat transfer, the left hand side of the heat equation Eq. (2.107) is zero. Then, the Equation reduces to

$$\nabla \cdot (k(\vec{r}, t) \nabla T(\vec{r}, t)) = -Q_s(\vec{r}, t). \quad (2.108)$$

This shows that the resulting temperature distribution only depends on the thermal conductivity of the system, initial and boundary conditions and sources/sinks.

2.5 Finite element method

Solving physical problems related to heat transfer typically involves partial differential equations, such as the heat equation Eq. (2.107). Analytically, this equation is solvable only for specific problems with relatively non-complex geometrical structures and/or symmetries, such as cylinders, spheres and rectangles/cubes. For more complex geometries, it gets increasingly difficult to find an exact solution and one turns to numerical methods. The perhaps most used approach is the FEM, which gives an approximate solution of the problem.

Step one in the Finite Element Analysis (FEA) is to create a digital model of the physical system under investigation which resembles the real structure to a certain level of detail. Then, the discretization of the system is worked

out, better known as the process of meshing. Here, the system is divided into smaller spatial parts called finite elements, from which this method has its name. The shapes of these elements can range from 1D line elements to 3D elements such as tetrahedra or prisms.

Within the created finite elements and on their boundaries, there is a finite number of points called nodes to which the physical parameters are assigned. For the use in this thesis, the meshes were built using quadratic tetrahedrons. Here, there is one node in each corner and one on each midpoint between two corners, yielding ten nodes per element. These points are the discrete points at which the independent variables are computed, and the number of degrees of freedom, given in most cases by the amount of independent variables times the total number of nodes in the model, gives the number of equations that need to be solved. In simulations of linear piezoelectrics in the frequency domain, say for the \mathbf{d} -form Eqs. (2.32) and (2.33), there are in general six independent variables for the stress \vec{T} (Voigt notation) and three independent variables for the electric displacement \vec{D} . For steady-state heat transfer, the temperature T is the only independent variable.

To solve for the independent variable, one must obtain a set of equations at each node. Between subsequent nodes, interpolation functions are used to give intermediate values. For linear (quadratic) elements, these are linear (quadratic) with respect to the local coordinates in each element. At each node, material properties, boundary conditions and information about neighbouring nodes are given. For a small subdomain, one uses a linear combination of trial functions. The number of trial functions needed to represent the solution here is finite and together with their coefficients, which are to be computed, the functions give an approximate solution on the subdomain. The goal is to determine the coefficients of these functions so that the local error becomes as small as possible, usually performed by iterative algorithms. Finally, the local equations are combined into a global system matrix from which the independent variables are solved for.

One remark about the spatial discretization is necessary. An important parameter reflecting the model size and computation time is the number of nodes. The denser the mesh, that is the higher the number of elements per unit volume, unit area or unit length, the more nodes and hence the more equations. Indeed, the mesh density has a direct connection to the accuracy of the solution obtained, but beyond a certain point, further reductions in

element sizes and hence increase in the number of nodes will not give more accurate results. That is, the solution has converged and now only the number of calculations are increased without making any important difference in the solution. For this reason, it is convenient to do a mesh refinement study in which one investigates the effect of different mesh sizes and element types before deciding for a certain mesh for the model.

Chapter 3

Method: FEM modeling

Here, all aspects of the finite element modeling in COMSOL Multiphysics will be presented.

First, the modeling approach and relevant measures of the composites are presented in Section 3.1.

Second, in Section 3.2, 12 piezocomposites are picked and the materials of the composites and how they are modeled in COMSOL, including losses, will be discussed. Boundary conditions are specified and guidelines for the meshing are worked out. Moreover, the frequencies for which the simulations will be performed are given and all relevant physical quantities for discussion and comparison will also be presented.

Thirdly, following the same structure as before, electrodes and a quarter-wavelength matching layer are introduced in the model of one of the composites above. Additionally, a water load is added to the matching layer. This equals to Section 3.3.

Lastly, in Section 3.4, the steady-state heat transfer model of the composite with matching layer, electrodes and water load is presented with the choices of boundary conditions.

3.1 Unit cell modeling

The unit cell modeling approach for FEM modeling of 1-3 piezocomposites is very often motivated because it exploits periodicity and symmetry in order to reduce the computational problem significantly. In the literature, it is extensively used for purposes such as determination of the electrical impedance spectrum and electromechanical efficiency [16, 17, 5] of 1-3/2-2 composites, to mention some. In [5], the method has also been compared

with FEM simulations of finite-sized composites and experimental results. It was concluded that the unit cell approach underestimated the resonance frequency compared to the frequency obtained experimentally for high ceramic aspect ratios ($w_r/t_c > 0.4$) and that the simulations of finite-sized composites were the most accurate for such high aspect ratios. However, the latter simulations were performed using a 2D-model, which gives a huge speed-up compared to a simulations taking all three spatial dimensions into account. As the computational demands for a finite-sized 3D composite quickly grow out of proportion and sufficient computational resources were not available, the unit cell model approach is selected for this thesis. An important consequence of this choice is that one loses information about resonance modes that occur for a finite-sized composite, such as those caused by the width of the composite as a whole.

In this thesis, as in the discussion in Subsection 2.3.1, the periodicity of the composite will be assumed to be the same along both lateral directions and square pillars are used. Then, the unit cell approach permits further reduction of the model size if accompanied with appropriate boundary conditions. To visualize this, consider Fig. 3.1. Here, a portion of a 1-3 composite is viewed from above with the borders of four unit cells illustrated. The lower left unit cell is subdivided into four equal *quarter* unit cells by two planes of symmetry. Hence, modeling a unit cell with periodic boundary conditions is equivalent to analyzing a quarter cell with mirror symmetry conditions. Both amount to infinite transversely periodic structures.

Further inspection of Fig. 3.1 yields that the upper surface area of a unit cell is $(w_r + \Delta w_r)^2$ and that the PZT area fraction of that area is the same as the PZT volume fraction of a unit cell ν since the thickness of the epoxy and PZT rods t_c is the same:

$$\nu = \frac{w_r^2}{(w_r + \Delta w_r)^2}. \quad (3.1)$$

This clearly also holds for quarter unit cells, as both the numerator and the denominator scale with a factor of 1/4. For a given ν and rod size w_r , the rod spacing Δw_r (see Fig. 2.2 or Fig. 3.1) can be found by solving for it in Eq. (3.1):

$$\Delta w_r = w_r \left(\frac{1}{\sqrt{\nu}} - 1 \right). \quad (3.2)$$

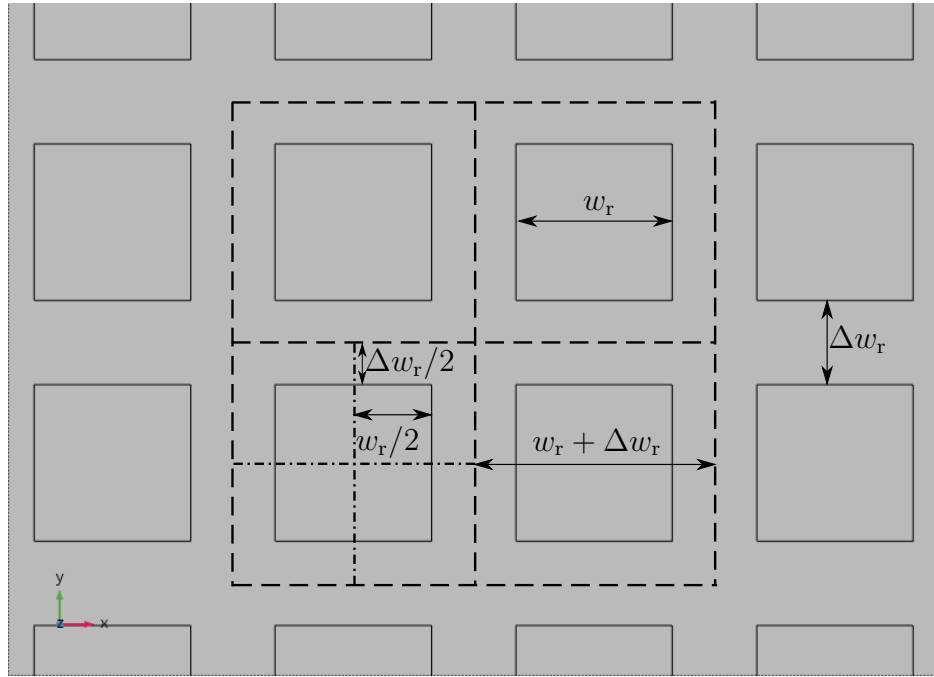


Fig. 3.1: A portion of a 1-3 composite as shown in Fig. 2.1 seen from above with the borders of four neighboring unit cells (dashed lines). One can imagine that cutting the composite all the way through in the thickness direction along these borders would give four replicas of the unit cell. Moreover, further cutting one unit cell along its indicated planes of symmetry (dot-dashed lines) would result in four *quarter* unit cells. The width of the epoxy in a unit cell is depicted, namely $\Delta w_r/2$, later also referred to as the epoxy half-width. From this Figure, it is clear that the periodicity is $w_r + \Delta w_r$.

The pillar aspect ratio (AR) is also given:

$$AR = \frac{w_r}{t_c}. \quad (3.3)$$

3.2 1-3 piezocomposites in vacuum

3.2.1 Dimensions of the unit cells

In total, four volume fractions and three rod sizes were chosen. For each volume fraction, the same three rod sizes were picked for purposes of comparison. The configurations obtained are characterized in Table 3.1 by their volume fraction ν , rod size w_r , rod spacing Δw_r and pillar aspect ratio AR. It is clear that three configurations have pillar aspect ratios as high as 0.5 and these composites may have their lateral resonances occurring close to the thickness resonances. For piezocomposites operating in thickness mode, this is, as pointed out in Subsection 2.3.2, not favourable, so these composites are considered for the purpose of investigating the power dissipation. Moreover, the pillar size of 10.0 mm actually becomes comparable to the shortest wavelength of body waves propagating in the composite. A shear wave in the epoxy would at a driving frequency of $f = 110\,000$ Hz have a wavelength $\lambda \approx 12.9$ cm. Hence, the correspondence with the effective medium model with respect to thickness resonance frequencies is expected to be the poorest for these composites due to the high pillar aspect ratio AR and wide pillar spacing Δw_r compared to the pillar size w_r .

3.2.2 Materials and losses

For the piezoelectric, EC-69 manufactured by EDO (acquired by Harris) was chosen. It is a hard doped PZT, which in general is characterized by higher piezoelectric coupling and electrical permittivities compared to soft doped PZTs and is applicable for high power transmission [18], the latter property making it suitable for the uses in this thesis.

As electric excitation of the material gives rise to power dissipation and heating, its temperature increases. Compared to soft PZTs, hard doped PZTs often show more temperature stability in their material properties relative to soft PZTs [18]. The temperature dependence of this particular PZT has been studied for a wide range of temperatures [19]. For the temperature interval of interest in this thesis, namely 15 °C to 40 °C, it seems to be a good approximation to use temperature independent material coefficients.

Table 3.1: PZT volume fraction ν , rod size w_r , rod spacing Δw_r determined by Eq. (3.2) and pillar aspect ratio AR for the 12 composites considered. The thickness $t_c = 20$ mm of the composite is fixed. For the definitions of w_r and Δw_r , see Fig. 2.2.

no.	ν	w_r (mm)	Δw_r (mm)	AR
1	40 %	3.5	2.0	0.175
2	40 %	6.0	3.5	0.3
3	40 %	10.0	5.8	0.5
4	50 %	3.5	1.4	0.175
5	50 %	6.0	2.5	0.3
6	50 %	10.0	4.1	0.5
7	60 %	3.5	1.0	0.175
8	60 %	6.0	1.7	0.3
9	60 %	10.0	2.9	0.5
10	80 %	3.5	0.4	0.175
11	80 %	6.0	0.7	0.3
12	80 %	10.0	1.2	0.5

The relevant material data was acquired at a temperature of 15 °C in [19], also taking into account the losses via complex notation as in Eqs. (2.46)-(2.48). As COMSOL supports complex material coefficients, these can be used directly. All relevant material data is provided in Appendix B.

For the piezoelectric inactive material in the composite, the epoxy as described in [20] was picked. Its material properties are characterized at room temperature, including the mechanical quality factor Q_m . Thus, all the necessary data is provided to model this epoxy as a linear elastic isotropic material with mechanical losses given through the complex elastic stiffness matrix (generalization of Eq. (2.24)). However, since the losses are isotropic and the elastic stiffness matrix cannot be typed in directly for a linear elastic material in COMSOL, the easiest approach in COMSOL is to specify a so-called isotropic structural loss factor $\eta = Q_m^{-1}$. Then, COMSOL interprets the elastic stiffness as

$$c_{\alpha\beta} = c'_{\alpha\beta}(1 + i\eta), \quad (3.4)$$

where $c'_{\alpha\beta}$ is the real value of the elastic stiffness coefficients, in COMSOL

calculated given the Young's modulus E and Poisson's ratio σ [9]:

$$c'_{11} = \frac{E(1 - \sigma)}{(1 + \sigma)(1 - 2\sigma)}, \quad (3.5)$$

$$c'_{12} = \frac{E\sigma}{(1 + \sigma)(1 - 2\sigma)}, \quad (3.6)$$

$$c'_{44} = \frac{c'_{11} - c'_{12}}{2} = \frac{E}{2(1 + \sigma)}. \quad (3.7)$$

In addition, the density ρ is needed to calculate, for instance, the longitudinal and shear wave velocities Eqs. (2.14) and (2.15). So all in all, the material parameters needed to model the epoxy as a lossy linear elastic isotropic material are the Young's modulus E , the Poisson's ratio σ , the density ρ and the mechanical quality factor $Q_m = \eta^{-1}$, all listed in Appendix B. Last but not least, though the electrodes were not modeled, it was fair to include the dielectric properties of the epoxy in the simulation as the voltage would be applied uniformly over the entire upper and lower surface of the quarter unit cell. The relative permittivity and dielectric loss angle were given in [20], so the epoxy was modeled as a linear dielectric with isotropic permittivity. These values are then also provided in Appendix B.

3.2.3 Boundary conditions

Modeling only a quarter unit cell, symmetry boundary conditions needed to be applied to all external surfaces of the quarter cell, except for the top and bottom, where stress free boundary conditions were applied (vacuum). For a surface with outward normal \vec{n} , the mathematical expression for the symmetry boundary condition is given by

$$\vec{\xi} \cdot \vec{n} = 0, \quad (3.8)$$

$\vec{\xi}$ denoting the displacement on the surface. Stress free boundaries corresponds to, as the name suggests,

$$T_{\alpha\beta} = 0 \quad (3.9)$$

on the applicable surfaces. Finally, to electrically excite the quarter unit cell, its lower surface was grounded and a sinusoidal varying voltage with frequency f was applied to the upper surface with peak voltage $V_0 = 10$ V. The relevant frequencies will be determined in Subsection 3.2.5.

3.2.4 Meshing considerations

To ensure that the finite element solutions were accurate enough, a mesh refinement study was performed. As a rule of thumb in general, the number of elements per shortest wavelength of waves propagating in the media should be at least 6, so this was used as a starting point. The shortest wavelength was, as used in Subsection 3.2.1, that of shear waves in the epoxy, given by the shear wave velocity divided by the highest frequency sampled. However, the obtained mesh size was found to be too coarse when performing initial analyses. In particular, some guidelines on the mesh that were applied to all 12 quarter cells were developed based on the mesh refinement study:

1. Automatically generated meshes consisting of tetrahedral elements were favoured over automatically generated meshes consisting of hexahedral elements with respect to fulfillment of stress free boundary conditions and computational effort necessary to reach sufficient convergence.
2. The number of elements per shortest wavelength λ_{\min} should be at least 15.
3. The number of elements along the half-width $\Delta w_r/2$ of the epoxy should be at least 2.
4. Due to limited computational power, the total number of elements in the quarter cell should not be much larger than 40 000.

Elaborating on the first guideline, it was found that although stress free boundary conditions Eq. (3.9) (called "Free" in COMSOL) were applied to the upper and lower surface of the unit cell facing vacuum, there could still be non-zero stresses occurring, in particular close to the boundaries of the quarter cell. However, evaluating the zz -component of the stress along a transverse line at the material boundary between the epoxy and PZT revealed that the stress reduced towards the intersect with the plane of symmetry (see Fig. 3.1). One convergence criterion was based on the reduction of these stresses with decreasing mesh size. A second criterion was based on the relative change in quantities like stress, strain and electric displacement field along lines in the thickness direction, running all the way through the composite. Sufficient convergence was reached when these quantities displayed changes by only a few percent upon further reductions of the mesh size and when the stresses along the material boundary rapidly decreased

to zero compared to the stresses with coarser mesh sizes. Not only did the tetrahedral elements show the best performance for the latter as the mesh size decreased, but they were also superior in terms of computational effort. Hence, this element shape was chosen.

In the first guideline, it also needs to be clarified how "automatically generated meshes" are produced. In COMSOL, there are predefined mesh settings and the settings for "extremely fine" were used, changing only the predefined minimum and maximum element sizes. From these, a tetrahedral mesh was built.

The second and third guidelines were based on the mesh refinement study as well. Although the rod size w_r was repetitive (see Table 3.1), the rod spacing Δw_r (epoxy) was not because it was changed to acquire the correct volume fraction (Eq. 3.2). Consequently, the volume of the quarter cells changed, so the mesh sizes had to be adjusted for each quarter cell to obtain a sufficiently fine mesh on which the dependent variables could be solved for within a reasonable time frame. This is why the last guideline was also introduced.

Fig. 3.2 and Fig. 3.3 show the mesh on the upper surface of the quarter unit cell based on composite no. 3 and 10 in Table 3.1, respectively. In Fig. 3.4, the first mesh is displayed for the entire quarter cell. In Table 3.2, the shortest wavelength λ_{\min} , the number of elements per λ_{\min} , the number of elements along the half-width of the epoxy $\Delta w_r/2$, the total number of elements and the number of degrees of freedom for the meshes of the quarter unit cells with dimensions given in Table 3.1 are presented. Overall, most of the meshes have their total number of elements close to 40000 as given in guideline no. 4, but especially quarter unit cell no. 10 has a very high amount. This is explained by the fact that the rod spacing is the smallest for this composite (see Table 3.1), so the elements in the epoxy have to be correspondingly smaller to meet guideline no. 3 of at least 2 elements per half-width (column no. 6 in Table 3.2). Thus, the number of elements increases.

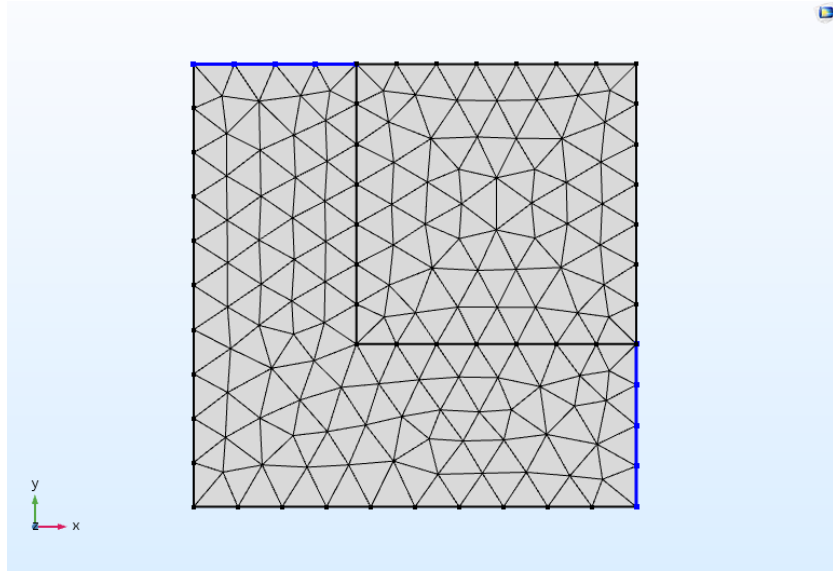


Fig. 3.2: Mesh of the quarter cell representation of composite no. 3 in Table 3.1 (volume fraction $\nu = 0.4$ and rod size $w_r = 3.5$ mm), seen from above. 4 tetrahedral elements can be counted along the indicated lines (blue), which have lengths corresponding to the epoxy half-width $\Delta w_r/2$.

3.2.5 Determination of sampling frequency and frequency domain

From the effective medium model, one expects the series and parallel resonances to develop at higher frequencies for higher volume fractions. However, this model does not distinguish between composites of different lateral spatial scales - it is only assumed that they are sufficiently fine. Preliminary finite element simulations for coarser mesh sizes showed that the resonance frequencies were also dependent on such dimensions. More precisely, for a fixed volume fraction ν , increasing rod sizes w_r gave decreasing resonance frequencies, but the differences were only of the order of a few thousand hertz. Thus, quarter cells of the same volume fraction were driven at the same frequencies, also appropriate for purposes of comparison later. Based on the resonance frequencies obtained for coarser meshes and the effective medium model, the frequency domains to be sampled were determined. For all quarter cells, 101 equally spaced frequencies were sampled with a sampling frequency of

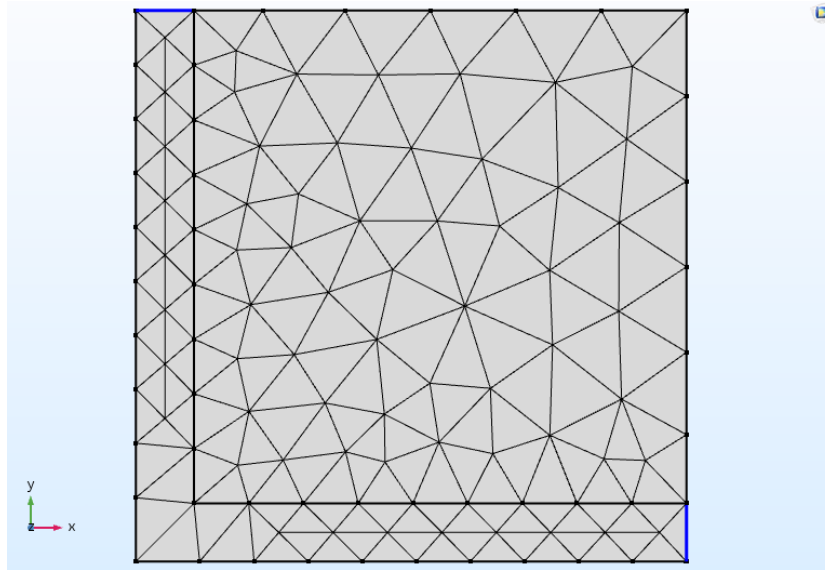


Fig. 3.3: Mesh of the quarter cell representation of composite no. 10 in Table 3.1 (volume fraction $\nu = 0.8$ and rod size $w_r = 3.5$ mm), seen from above. 1 tetrahedral element can be counted along the indicated lines (blue), which have lengths corresponding to the epoxy half-width $\Delta w_r/2$. However, it is clear that there are mostly 2 elements along the epoxy half-width. Also notice how the element density in the PZT increases close to the boundary between the two domains to combine on the material domain boundaries. As a result, the mesh in the PZT becomes finer closer to the epoxy.

400 Hz, thus covering a frequency interval of length 40 000 Hz. The minimum and maximum frequencies sampled f_{\min} and f_{\max} are given with the mesh related parameters in Table 3.2. These intervals are only large enough to give the fundamental resonances. Higher order resonances will not be considered but lateral modes, if they occur within the given interval, will be.

3.2.6 Physical quantities of interest

Starting with the power dissipation, the total power dissipation in a quarter unit cell was defined as the volume integral of Holland's power dissipation

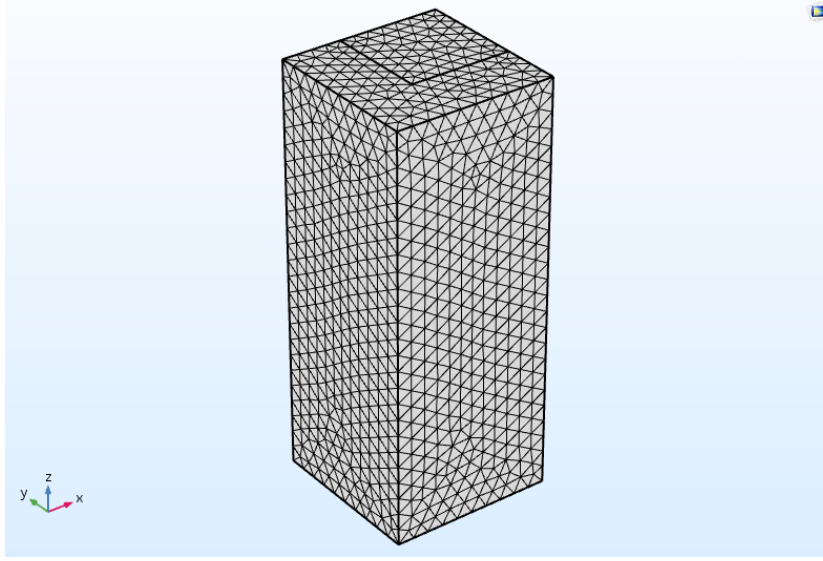


Fig. 3.4: Mesh of the quarter unit cell representation of composite no. 1 (volume fraction $\nu = 0.4$ and rod size $w_r = 3.5$ mm), seen from the side.

density P_d Eq. (2.45) over the quarter unit cell \mathcal{V} :

$$P(\omega) = \iiint_{\mathcal{V}} P_d(\vec{r}, \omega) d\mathcal{V} = \frac{1}{2}\omega \iiint_{\mathcal{V}} \text{Im}\left\{\vec{E} \cdot \vec{D}^* + \mathbf{T} : \mathbf{S}^*\right\} d\mathcal{V}. \quad (3.10)$$

\vec{r} is a position vector. In COMSOL, the stress and strain tensor and the electric field and displacement field are all defined, so P_d can be defined as a variable to be numerically integrated over the mesh of the quarter unit cell. It is also interesting to compute the average power dissipation per unit volume. However, since all quarter unit cells considered have the same thickness t_c , it suffices to calculate the power dissipation P_A per quarter cell unit area A :

$$P_A(\omega) = \frac{1}{A} \iiint_{\mathcal{V}} P_d(\vec{r}, \omega) d\mathcal{V} = \frac{P(\omega)}{A} \quad (3.11)$$

By Fig. 3.1, or just Eq. (3.1), it is clear that $A = \frac{1}{4}(w_r + \Delta w_r)^2$.

Furthermore, the total power dissipation $P(\omega)$ in the piezocomposite as a whole can be seen to be composed of two terms, one for the epoxy and one

Table 3.2: Overview of the minimum and maximum frequencies sampled f_{\min} and f_{\max} , the shortest wavelength of shear waves in epoxy λ_{\min} , the minimum number of elements per shortest wavelength ($\# \text{ el.}/\lambda_{\min}$), the number of elements along the half-width of the epoxy ($\# \text{ el.}/\frac{\Delta w_r}{2}$), the approximate total number of elements in the quarter cell ($\# \text{ el.}$) and finally the approximate number of degrees of freedom ($\# \text{ d.o.f.}$). A sampling frequency of $\Delta f = 400 \text{ Hz}$ was used for all composites.

no.	f_{\min} (Hz)	f_{\max} (Hz)	λ_{\min} (mm)	$\# \text{ el.}/\lambda_{\min}$	$\# \text{ el.}/\frac{\Delta w_r}{2}$	$\# \text{ el.}$	$\# \text{ d.o.f.}$
1	70 000	110 000	12.9	31.8	3	35 000	196 000
2	70 000	110 000	12.9	23.4	3	42 000	235 000
3	70 000	110 000	12.9	16.1	4	40 000	224 000
4	70 000	110 000	12.9	37.9	2	49 000	274 400
5	70 000	110 000	12.9	23.4	3	35 000	196 000
6	70 000	110 000	12.9	16.1	3	31 000	174 000
7	80 000	120 000	11.8	34.7	2	36 000	202 000
8	80 000	120 000	11.8	23.6	2	33 000	185 000
9	80 000	120 000	11.8	15.9	2	31 000	174 000
10	90 000	130 000	10.9	36.3	2	62 000	347 000
11	90 000	130 000	10.9	19.8	2	38 000	213 000
12	90 000	130 000	10.9	14.1	2	28 000	157 000

for the PZT:

$$P(\omega) = P_{\text{PZT}} + P_e \quad (3.12)$$

$$= \iiint_{\mathcal{V}_{\text{PZT}}} P_d(\vec{r}, \omega) d\mathcal{V} + \iiint_{\mathcal{V}_e} P_d(\vec{r}, \omega) d\mathcal{V}. \quad (3.13)$$

Dividing by the total power dissipation $P(\omega)$ yields the relative power dissipation Π in each domain:

$$1 = \Pi_{\text{PZT}} + \Pi_e. \quad (3.14)$$

This concludes the discussion on quantities related to the power dissipation. Below, the resonance frequencies and electrical impedance $Z(\omega)$ will be considered.

To identify the series f_s and parallel resonance frequency f_p in COMSOL, it was convenient to first calculate the admittance $Y(\omega)$ by [1]

$$Y(\omega) = \frac{1}{Z(\omega)} = G(\omega) + iB(\omega) = \frac{i\omega}{V_0} \iint_{\mathcal{A}} \vec{D}_{\perp}(\vec{r}, \omega) \cdot d\vec{A}. \quad (3.15)$$

The integral is the surface integral over the upper quarter cell surface \mathcal{A} (see Fig. 3.2 or Fig. 3.3) of the displacement field \vec{D}_{\perp} normal to the quarter cell surface. This gave the conductance $G(\omega)$ (real part) and admittance $B(\omega)$ (imaginary part) and the frequency of maximum conductance was then f_s by Subsection 2.3.2. To obtain f_p , the inverse of $Y(\omega)$ was computed to retrieve the impedance $Z(\omega)$ with resistance $R(\omega)$ (real part) and reactance $X(\omega)$ (imaginary part):

$$Z(\omega) = R(\omega) + iX(\omega). \quad (3.16)$$

According to the definition in Subsection 2.3.2, the frequency of maximum resistance $R(\omega)$ corresponded to f_p . The complex phase $\delta(\omega)$ of the impedance was also computed as

$$\delta(\omega) = \text{atan2}(X(\omega), R(\omega)). \quad (3.17)$$

It is also necessary to address a few details about the implementation of the effective medium model. As the effective medium model is based on the piezoelectric equations with stress \vec{T} (Voigt notation) and electric displacement \vec{D} as independent variables (\mathbf{e} -form) and the material coefficients of the PZT was given with respect to the \mathbf{d} -form (see Appendix B), the coefficients needed to be converted to the \mathbf{e} -form before application. This was done by following these three steps:

1. First, write the stiffness matrix \mathbf{c}^E under short-circuit conditions with symmetry as given in Eq. (2.39) and invert it to obtain the compliance matrix \mathbf{s}^E under short-circuit conditions.
2. Second, use Eq. (A.8) to compute the piezoelectric coefficient \mathbf{e} , with the piezoelectric coefficient \mathbf{d} given by Eq. (2.37).
3. Finally, compute \mathbf{e}^S by Eq. (A.14), using \mathbf{e}^T as given by Eq. (2.38).

The obtained resonances \bar{f}_s and \bar{f}_p from the effective medium model could then be compared to f_s and f_p found by the FEM analyses. For comparison

purposes, the relative difference δf_p (δf_s) of the parallel (series) resonance frequency obtained in COMSOL f_p (f_s) with respect to the parallel (series) resonance frequency acquired by the effective medium model \bar{f}_p (\bar{f}_s) are defined below:

$$\delta f_p = \frac{f_p - \bar{f}_p}{\bar{f}_p} \quad (3.18)$$

$$\delta f_s = \frac{f_s - \bar{f}_s}{\bar{f}_s}. \quad (3.19)$$

The comparison will be presented in Table 4.1 in Chapter 4 and discussed in Chapter 5.

3.3 1-3 piezocomposite with electrodes, matching layer and water load

Here, the quarter unit cell model of composite no. 1 (rod size $w_r = 3.5$ mm and volume fraction $\nu = 0.4$) will be modified to include a quarter-wavelength matching layer and a water load. Electrodes will also be added on the top and bottom surfaces (with respect to the thickness direction) of the piezocomposite. The effect of such relatively thin but highly thermal conductive slabs, on the temperature increase obtained by the steady-state transfer simulation will be investigated in the Discussion. Ultimately, this four-layer structure (electrode, composite, electrode, matching layer) will be the geometry considered in the steady-state heat transfer analysis.

3.3.1 Dimensions of the unit cell

The quarter unit cell approach will still be used and since the matching layer will be modeled with the same lateral dimensions as the quarter unit cell, only its thickness t_{ML} needs to be calculated.

In Subsection 2.1.4, it was shown that perfect transmission (reflection coefficient $R = 0$) was achieved given that

1. the finite-sized medium had a thickness corresponding to that of a quarter-wavelength of the pressure waves propagating through the medium, and
2. its characteristic acoustic impedance was equal to the geometric mean of the surrounding media.

In fact, this also holds for a matching layer sandwiched between a composite and water load [1]. As the power reflection coefficient is the square of the reflection coefficient R in Eq. (2.17), maximum power transmission occurs as well for such situations. The matching layer thickness t_{ML} was chosen accordingly:

$$t_{\text{ML}} = \frac{\lambda}{4}. \quad (3.20)$$

The thickness was computed based on the series resonance frequency f_s of the 1-3 composite as defined in Eq. (2.59). Thus,

$$t_{\text{ML}} = \frac{v_{\text{ML}}}{4f_s}, \quad (3.21)$$

where v_{ML} is the longitudinal wave velocity in the matching layer (ML).

Copper-electrodes were added on the top and bottom of the composite with thicknesses of $t_{\text{Cu}} = 0.1$ mm.

A picture of a unit cell of the structure is shown in Fig. 3.5.

3.3.2 Materials and losses

It was searched in the literature for a matching material with characteristic acoustic impedance that was close as possible to

$$Z_{\text{ML}} = \sqrt{Z_{\text{comp.}} Z_{\text{water}}} \approx \sqrt{\bar{Z} Z_{\text{water}}}, \quad (3.22)$$

invoking the effective characteristic acoustic impedance \bar{Z} of the composite as given by the effective medium model Eq. (2.94) in Subsection 2.3.3. Excellent agreement was found with the a matching material given in Table III in [21]. Attenuation coefficients of longitudinal α_l and shear waves α_s had also been investigated and these were converted into Q -values Q_l and Q_s by rewriting

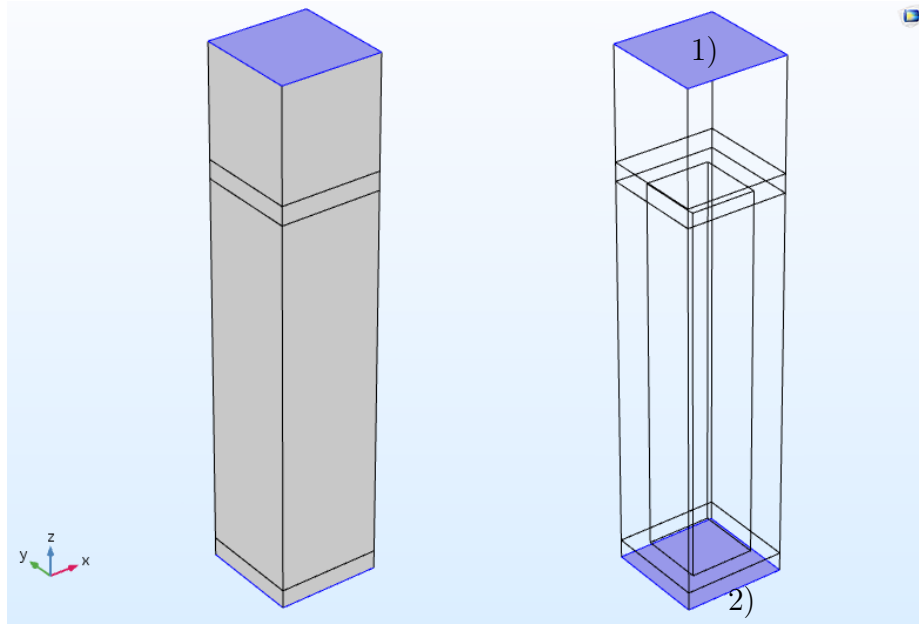


Fig. 3.5: A unit cell of a composite with electrodes (made thicker on purpose for better visualization) and matching layer. To the left, it is displayed with faces, while to the right, it is displayed without faces. In the latter, one can see the PZT rod embedded in the epoxy matrix. The numbers relate to the highlighted surfaces (blue). 1) Upper surface of the matching layer, onto which the water load is applied. In the steady-state heat transfer simulation, this is the surface onto which the constant temperature boundary condition is applied. 2) Lower surface of lower electrode, onto which the stress-free boundary condition is applied. In the steady-state heat transfer simulation, this is the surface onto which the convective heat transfer and possibly the thermal radiation boundary condition are applied (relevant for Subsection 3.4.1).

Eq. (2.21) in terms of the frequency f_0 (given in Appendix B) used in the characterization method in [21] and the wave velocities:

$$Q_i = \frac{\pi f_0}{v_i \alpha_i}, \quad i \in \{1, s\}. \quad (3.23)$$

Then, Eq. (2.23) was used to apply complex wave velocities in COMSOL, along with the density ρ . This was sufficient to describe the matching layer material as a lossy linear elastic isotropic material.

The electrodes consisted of copper and were modeled as linear elastic isotropic solids with material properties as given in the material library in COMSOL. By Eq. (2.18), the copper electrodes would appear almost acoustic transparent ($k_1 L \sim 10^{-2}$ at 130 000 Hz, the highest frequency), so they were not brought into the simulation to account for transmission effects. The reason why they were introduced at this point and not only for the steady-state heat transfer simulations was that it would make it easier to set up the heat simulations in COMSOL with regards to the heat sources. Since they were very thin, the extra computational effort necessary was negligible. Due to the same reason, they were also assumed to be lossless.

3.3.3 Boundary conditions and related assumptions

At all external surfaces, except for the top surface of the matching layer and the bottom surface of the lower electrode, the symmetry boundary condition Eq. (3.8) was applied. Like in the models with the composites in vacuum, the voltage was applied on the upper surface of the composite and the lower surface was grounded. As the electrodes were assumed to be lossless, the voltage would be the same if applied over the electrodes, so this was a valid assumption. The magnitude of the driving voltage was raised to $V_0 = 200$ V so that the power dissipation density applied as the heat source in the heat transfer simulations would yield a significant temperature rise. Moreover, the backing layer was assumed to be air. The ratio of characteristic acoustic impedance of the composite to air is $\sim 10^5 - 10^6$, so the acoustic transmission into this medium is negligible ($R \approx -1$ by Eq. (2.18)). Therefore, the backing layer was not modeled and a stress free-boundary condition (Eq. (3.9)) was applied to the lower surface of the lower electrode (see Fig. 3.5).

On the remaining external surface, namely the upper surface of the matching layer (see Fig. 3.5), the water load was modeled as a complex normal force per surface area F_\perp given by

$$F_\perp = -Z_{\text{water}} v_\perp, \quad (3.24)$$

where v_\perp is the complex velocity, evaluated at each node on the surface. This implicitly assumes that the sound power transferred into water is radiated parallel to the thickness direction. This is fair for thickness oscillations.

3.3.4 Meshing considerations

For the composite and the matching layer, the same mesh settings as used for the composite in vacuum were used. As the shear wave velocity in the matching layer was higher than that in the epoxy, the shortest wavelength of waves propagating in the matching layer would be longer than that in the epoxy, so using the same mesh size should be more than sufficient. On the electrodes, a swept mesh was applied in the thickness direction.

3.3.5 Physical quantities of interest

The total power dissipation in this case can be seen to be composed of four terms, one for each material. However, since the electrodes are assumed to be lossless, only the PZT, epoxy (e) and matching layer (ML) need to be accounted for. Eq. (3.13) is rewritten to also include the matching layer contribution P_{ML} :

$$\begin{aligned}
 P(\omega) &= P_{\text{PZT}} + P_e + P_{\text{ML}} \\
 &= \iiint_{\text{PZT}} P_d(x, y, z, \omega) dx dy dz \\
 &+ \iiint_e P_d(x, y, z, \omega) dx dy dz \\
 &+ \iiint_{\text{ML}} P_d(x, y, z, \omega) dx dy dz.
 \end{aligned} \tag{3.25}$$

Dividing by the total power dissipation yields the relative power dissipation Π in each domain:

$$1 = \Pi_{\text{PZT}} + \Pi_e + \Pi_{\text{ML}}. \tag{3.26}$$

As the purpose of this model was to investigate the power dissipation density and not to design a 1-3 piezocomposite transducer, parameters such as bandwidth, sensitivity and center frequency were of little importance. Neither were possible corrections to the thickness t_{ML} of the matching layer, which, depending on the application, may be necessary in order to optimize power transmission at the operating frequency of the transducer [15].

3.4 Steady-state heat transfer

For these simulations, the geometry is exactly the same as in the previous Section. As the simulations took less than a minute to run with the same mesh, it was simply kept the same. Thus, this Section only needs to address the boundary conditions and related assumptions.

3.4.1 Boundary conditions and related assumptions

First of all, *steady-state* heat transfer will be considered. This should be valid when the duty cycle of the transducer, which is the fraction of a period over which the transducer is electrically excited, is sufficiently high and the transducer transmits over a longer duration, or when the device transmits continuously (continuous wave, CW) [22].

Temperature dependence of the thermal conductivities will be neglected. The glass transition of the epoxy and matching layer is expected to happen at temperatures around $\sim 100^\circ\text{C}$, so this should be fair for these materials. Since the temperatures are only within 15°C to 40°C , the conductivity of PZT and copper should also undergo insignificant thermal fluctuations.

The mirror symmetry boundary conditions are applied to all external surfaces of the quarter unit cell except for the upper surface of the matching layer and lower surface of the lower electrode (see Fig. 3.5). In terms of heat transfer, these conditions read

$$\vec{q} \cdot \vec{n} = 0, \quad (3.27)$$

where \vec{q} is the heat flux and \vec{n} is the normal vector of the surface.

The piezocomposite with electrodes and matching layer is assumed to be submerged in sea water with a temperature of 15°C . Additionally, the relative motion between the transducer and sea water is taken to be sufficiently large so that the matching layer surface in contact with water has a constant temperature of 15°C . On the opposite end of the structure, convective heat transfer from the electrode into an air backing layer is assumed, the air kept at a higher temperature of 30°C due to expected heating from nearby electronics. Thermal radiation into the backing layer is disregarded, an assumption which will be validated in the Discussion. The convective heat

transfer boundary condition is given by

$$-\vec{n} \cdot \vec{q} = h(T_{\text{air}} - T), \quad (3.28)$$

where h is the convective heat transfer coefficient, T_{air} is the air temperature and T is the electrode surface temperature.

The next boundary condition is relevant for the discussion of possible temperature decrease due to thermal radiation from the lower electrode into an air backing layer. Assuming that the electrode is a diffuse emitter, meaning that it radiates thermal energy isotropically, and that the air backing layer is much thicker than the electrode, the thermal radiation boundary condition is given by

$$-\vec{n} \cdot \vec{q} = \epsilon_{\text{th}} \sigma_{\text{S-B}} (T_{\text{air}} - T)^4, \quad (3.29)$$

where ϵ_{th} is the emissivity, $\sigma_{\text{S-B}}$ is the Stefan-Boltzmann constant, T_{air} is the air temperature and T is the temperature of the radiating surface, namely the electrode.

Last but not least, homogeneous and isotropic thermal conductivities are used for all materials, their values given in Appendix B.

Chapter 4

Results

In this Chapter, the results are presented in the same order as the FEM models were given in the previous Chapter. Quantities relevant for comparison were first evaluated over a quarter unit cell and then normalized. All results will be discussed in the next Chapter.

4.1 1-3 composites in vacuum

Table 4.1: Parallel and series resonance frequencies of the twelve quarter unit cells obtained by FEM analyses and comparison with the corresponding resonance frequencies of the effective medium model [3] using the epoxy described in [20] and EC-69 PZT [14]. f_s : series resonance frequency obtained in COMSOL (frequency of maximum conductance). \bar{f}_s : series resonance frequency obtained by the effective medium model Eq. (2.100). f_p : parallel resonance frequency obtained in COMSOL (frequency of maximum resistance). \bar{f}_p : parallel resonance frequency obtained by the effective medium model Eq. (2.99). δf_p : relative difference in parallel resonance frequency as defined in Eq. (3.18). δf_s : relative difference in series resonance frequency as defined in Eq. (3.19).

no.	ν	w_r (mm)	f_s (Hz)	\bar{f}_s (Hz)	f_p (Hz)	\bar{f}_p (Hz)	δf_s	δf_p
1	0.4	3.5	88 400	84 400	103 600	102 200	4.7 %	1.4 %
2	0.4	6.0	87 200	84 400	102 000	102 200	3.3 %	-0.2 %
3	0.4	10.0	84 000	84 400	97 600	102 200	-0.5 %	-4.5 %
4	0.5	3.5	91 600	86 600	107 200	105 300	5.8 %	1.8 %
5	0.5	6.0	90 000	86 600	105 600	105 300	3.9 %	0.3 %
6	0.5	10.0	86 400	86 600	101 200	105 300	-0.2 %	-3.9 %
7	0.6	3.5	94 400	89 000	111 200	108 500	6.1 %	2.5 %
8	0.6	6.0	93 200	89 000	109 200	108 500	4.7 %	0.6 %
9	0.6	10.0	89 200	89 000	104 000	108 500	0.2 %	-4.1 %
10	0.8	3.5	106 800	98 400	124 000	118 700	8.5 %	4.5 %
11	0.8	6.0	105 200	98 400	121 600	118 700	6.9 %	2.4 %
12	0.8	10.0	100 400	98 400	115 600	118 700	2.0 %	-2.6 %

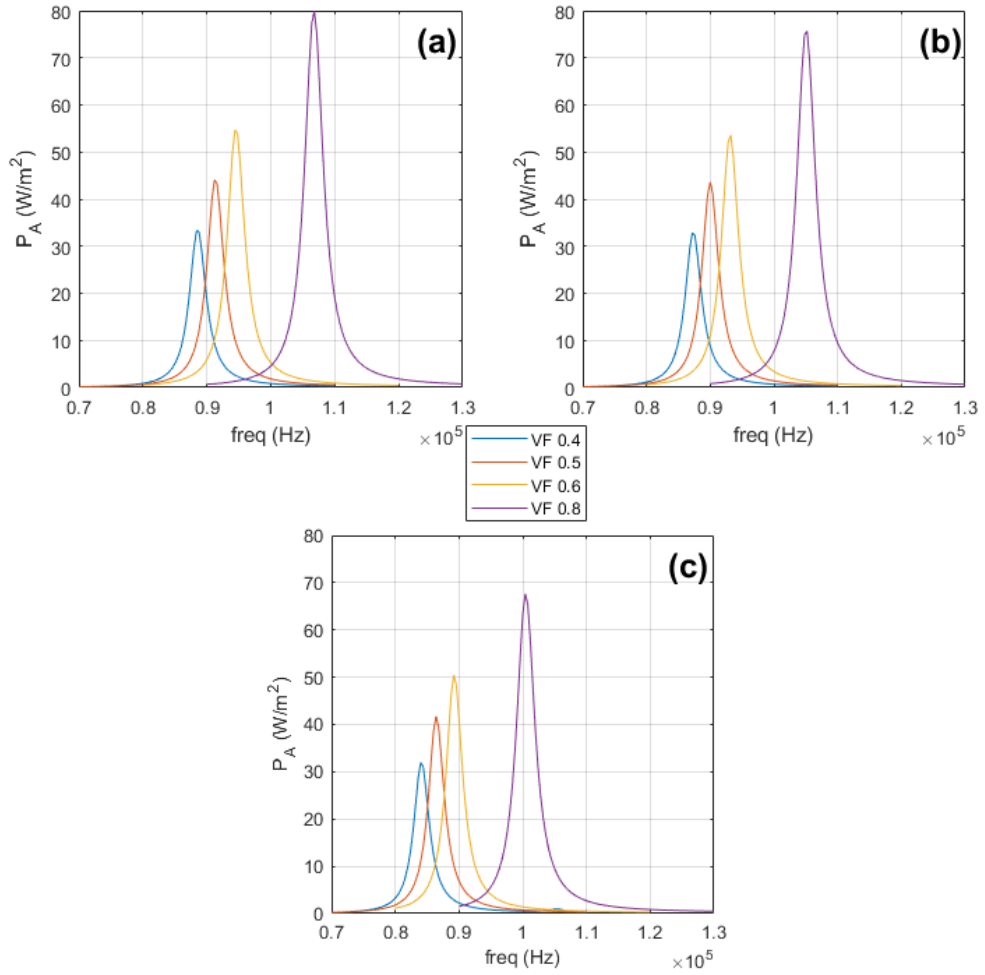


Fig. 4.1: Total power dissipation per surface area $P_A(f)$ as defined in Eq. (3.11), results grouped in terms of unit cell rod sizes w_r . (a) $w_r = 3.5$ mm, (b) $w_r = 6.0$ mm and (c) $w_r = 10.0$ mm. The amplitude of the drive voltage was $V_0 = 10$ V.

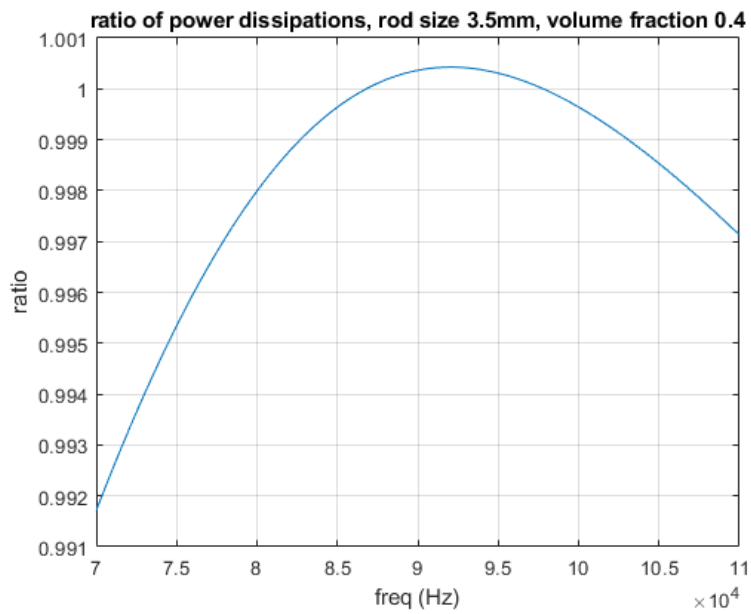


Fig. 4.2: Ratio of power dissipations given by Eq. (3.10) divided by Eq. (2.105). Here, the composite with rod size $w_r = 3.5$ mm and volume fraction $\nu = 0.4$ is considered only. Ideally, this should be a straight horizontal line of value 1 (see Subsection 2.3.4), but the discrepancies are sufficiently low (below 1%, as can be seen directly from the Figure), so these results are acceptable.

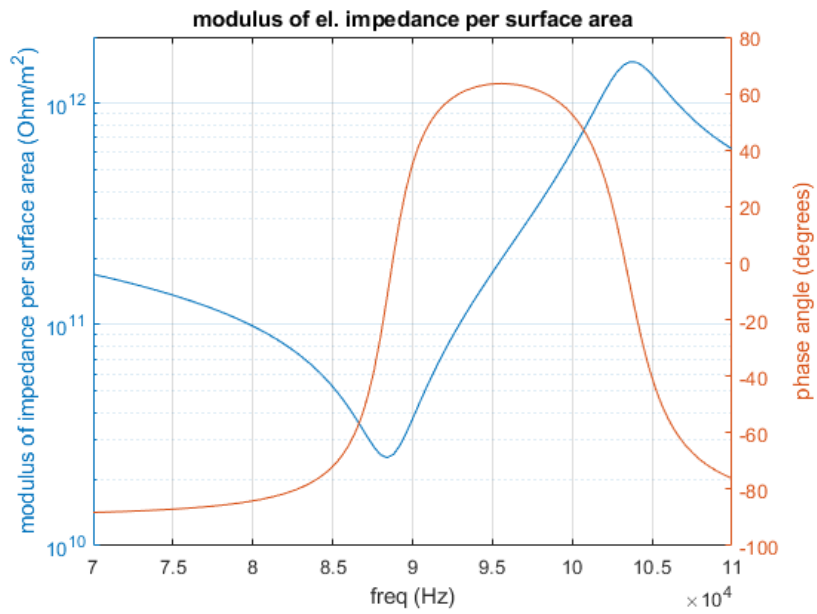


Fig. 4.3: Modulus of impedance normalized with respect to the quarter unit cell surface area A , $|Z(f)|/A$. $|Z(f)|$ was computed as the inverse of the admittance $|Y(f)|$ in Eq. (3.15). Here, $|Z(f)|/A$ is displayed for the 1-3 composite of rod size $w_r = 3.5$ mm and volume fraction $\nu = 0.4$. The phase angle $\delta(f)$ is also displayed. A peak voltage of $V_0 = 10$ V was used.

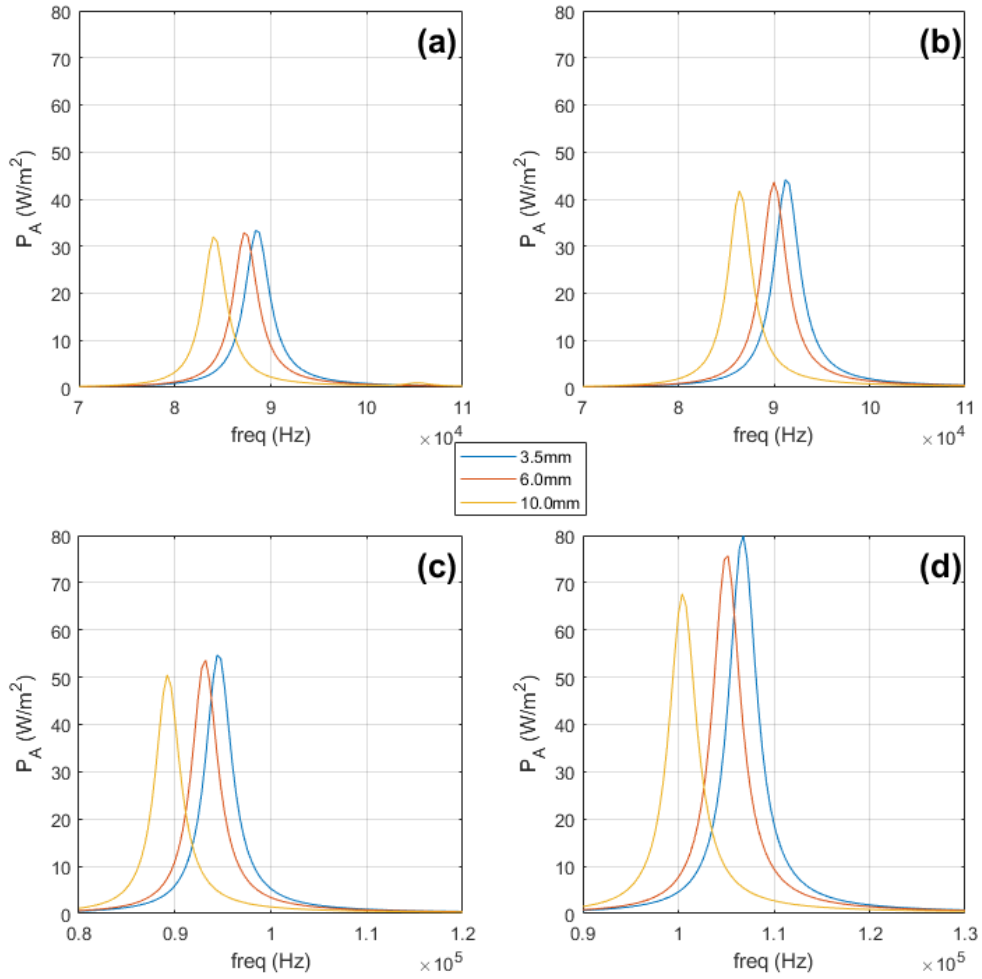


Fig. 4.4: Total power dissipation per surface area $P_A(f)$ as defined in Eq. (3.11), results grouped in terms of PZT volume fraction ν . (a) $\nu = 0.4$, (b) $\nu = 0.5$, (c) $\nu = 0.6$ and (d) $\nu = 0.8$. The amplitude of the drive voltage was $V_0 = 10$ V.

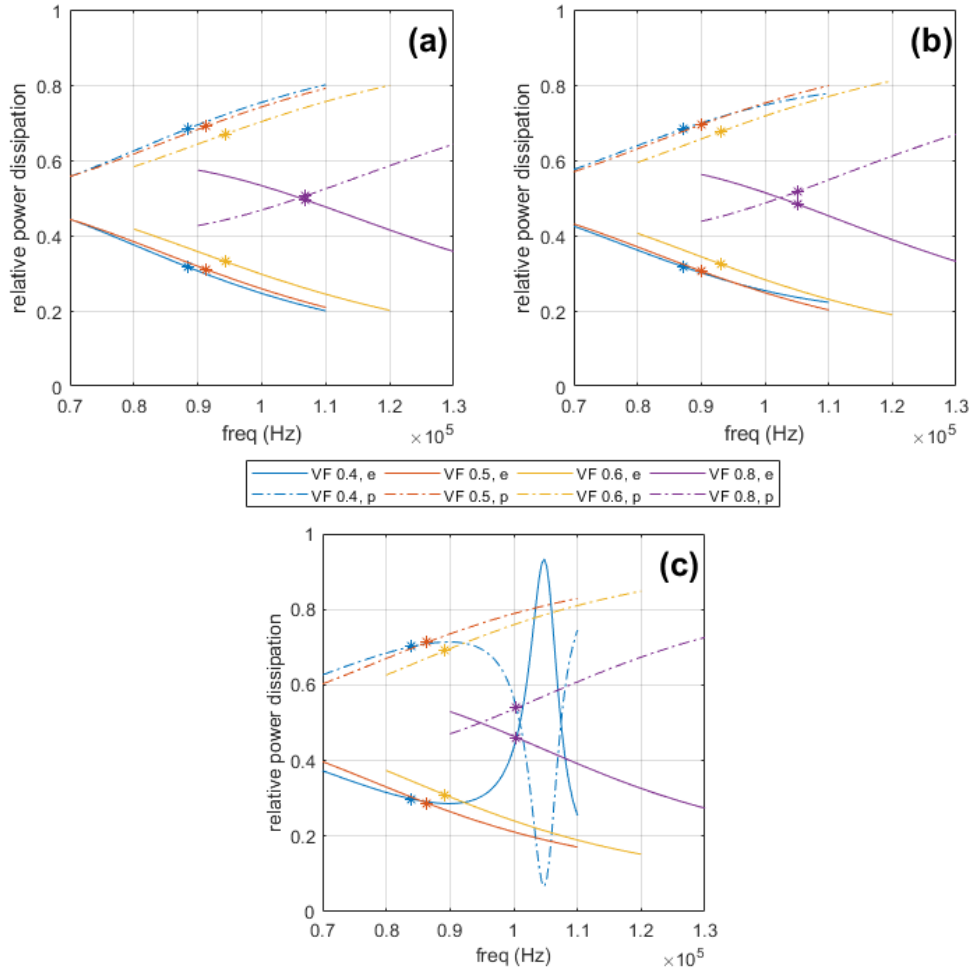


Fig. 4.5: Relative power dissipation of the epoxy (e, whole lines) Π_e and PZT (p, dash-dotted lines) Π_{PZT} as given by Eq. (3.14), results grouped in terms of unit cell rod sizes w_r . (a) $w_r = 3.5$ mm, (b) $w_r = 6.0$ mm and (c) $w_r = 10.0$ mm. The asterisks denote the respective values at resonance f_r .

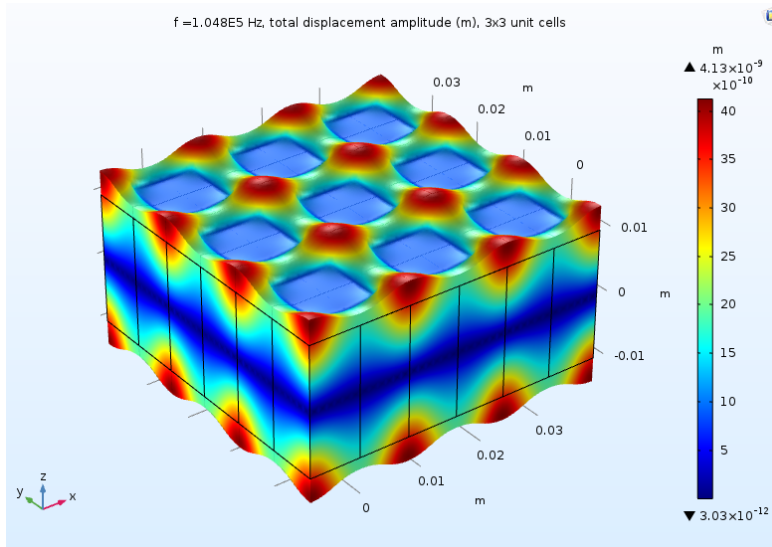


Fig. 4.6: Displacement amplitude $|\vec{\xi}|$ at $f = 104\,800$ Hz plotted for a 3×3 array of unit cells of rod size $w_r = 10.0$ mm and volume fraction $\nu = 0.4$. The spatial deformation is also shown, hugely exaggerated for purposes of visualization.

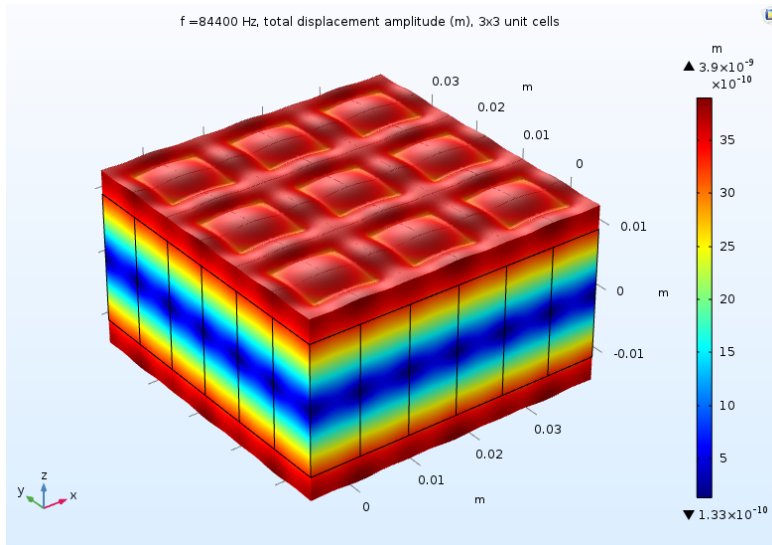


Fig. 4.7: Displacement amplitude $|\vec{\xi}|$ at thickness resonance $f_r = 84\,400$ Hz plotted for a 3×3 array of unit cells of rod size $w_r = 10.0$ mm and volume fraction $\nu = 0.4$. The spatial deformation is also shown, hugely exaggerated for purposes of visualization.

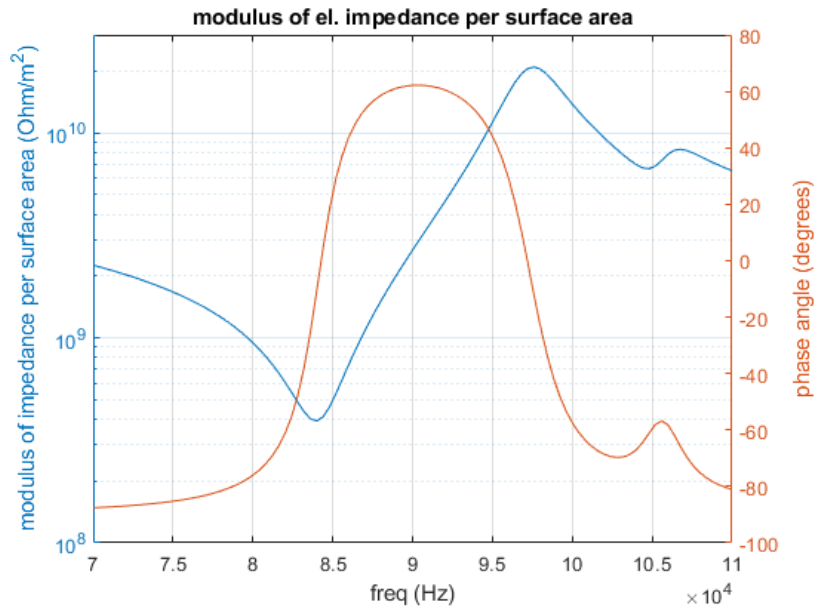


Fig. 4.8: Modulus of impedance normalized with respect to the quarter unit cell surface area A , $|Z(f)|/A$. $|Z(f)|$ was computed as the inverse of the admittance $|Y(f)|$ in Eq. (3.15). Here, $|Z(f)|/A$ is displayed for the 1-3 composite of rod size $w_r = 10.0$ mm and volume fraction $\nu = 0.4$. In contrast to Fig. 4.3, the quantity has two local maxima and two local minima, suggesting two types of resonances. The phase angle $\delta(f)$ is also displayed. A peak voltage of $V_0 = 10$ V was used.

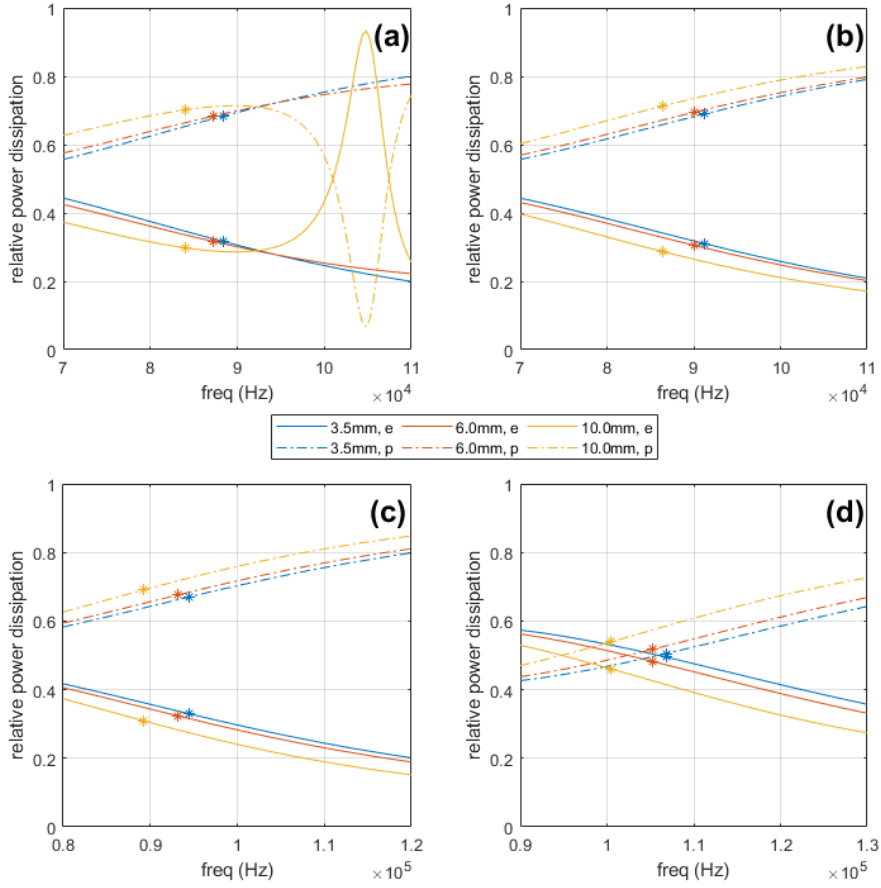


Fig. 4.9: Relative power dissipation of the epoxy Π_e and PZT Π_{PZT} as given by Eq. (3.14), results grouped in terms of PZT volume fraction ν . (a) $\nu = 0.4$, (b) $\nu = 0.5$, (c) $\nu = 0.6$ and (d) $\nu = 0.8$. The asterisks denote the respective values at resonance f_r .

4.2 1-3 composite with electrodes, matching layer and water load

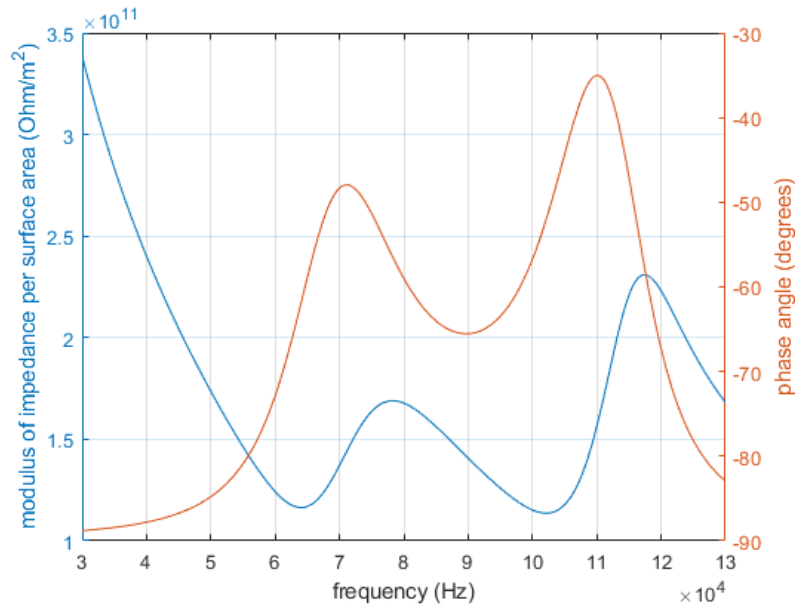


Fig. 4.10: Modulus of impedance normalized with respect to the quarter unit cell surface area A , $|Z(f)|/A$. $|Z(f)|$ was computed as the inverse of the admittance $|Y(f)|$ in Eq. (3.15). Here, $|Z(f)|/A$ is displayed for the 1-3 composite of rod size $w_r = 3.5$ mm and volume fraction $\nu = 0.4$ with electrodes, matching layer and water load. The phase angle $\delta(f)$ is also displayed. A peak voltage of $V_0 = 200$ V was used.

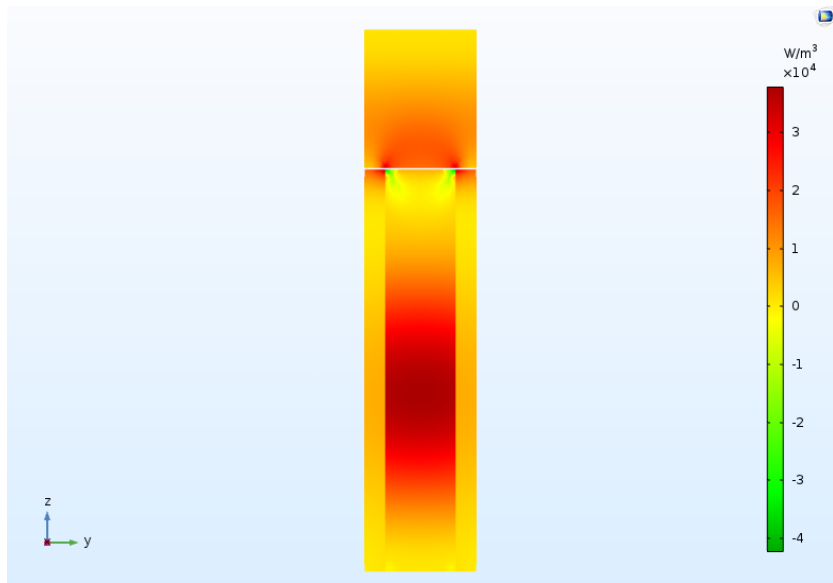


Fig. 4.11: Power dissipation density P_d as given by Eq. (2.45) plotted along the plane (of symmetry) $x = 0$ of a unit cell. The frequency considered is $f = f_{r2}$, defined in Table 5.1. Like in Fig. 3.5, the matching layer is seen in the upper portion of the plot, and the PZT below is surrounded with epoxy on both sides. A negative power dissipation density can be seen in some regions, which is not physical and is an artifact of FEM modeling.

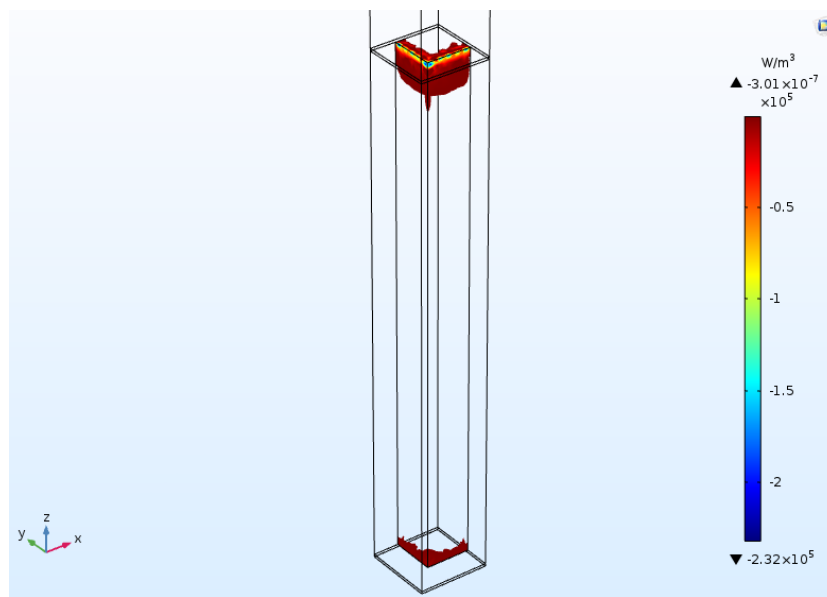


Fig. 4.12: Quarter unit cell, showing elements with one or more nodes where negative power dissipation density occurs. Only elements in the PZT display this property. Notice that the color bar has only negative values. Negative power dissipation density is not physical and is an artifact of FEM modeling.

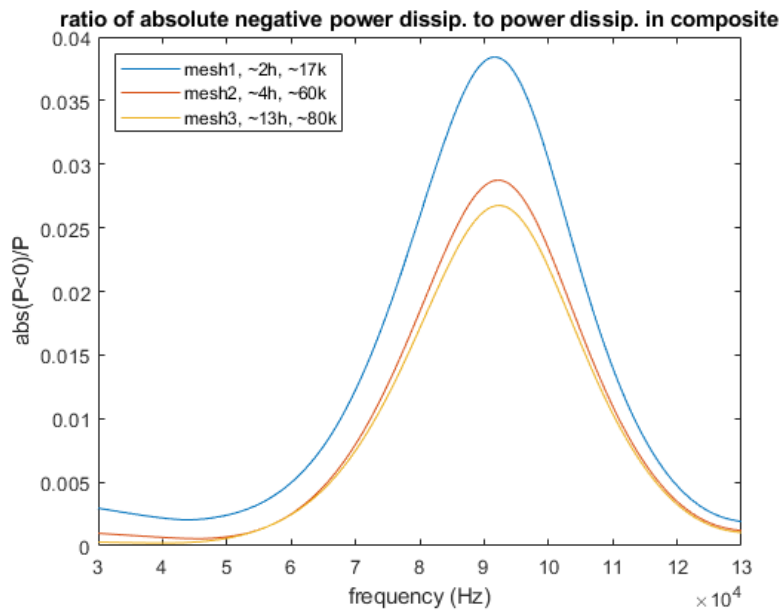


Fig. 4.13: Ratio of absolute negative power dissipation to power dissipation in composite, the latter given by Eq. (3.13), displayed for three different meshes with the approximate number of elements and simulation run time in hours given in the legend. Negative power dissipation is not physical and is an artifact of FEM modeling.

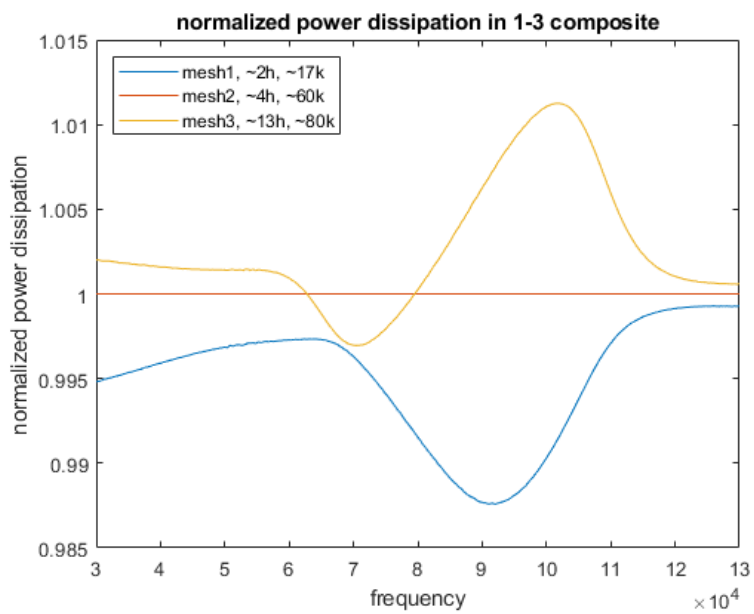


Fig. 4.14: Power dissipation in 1-3 composite given by Eq. (3.13) normalized with respect to power dissipation obtained running the simulation with mesh2. mesh2 was used as mesh to generate the results below.

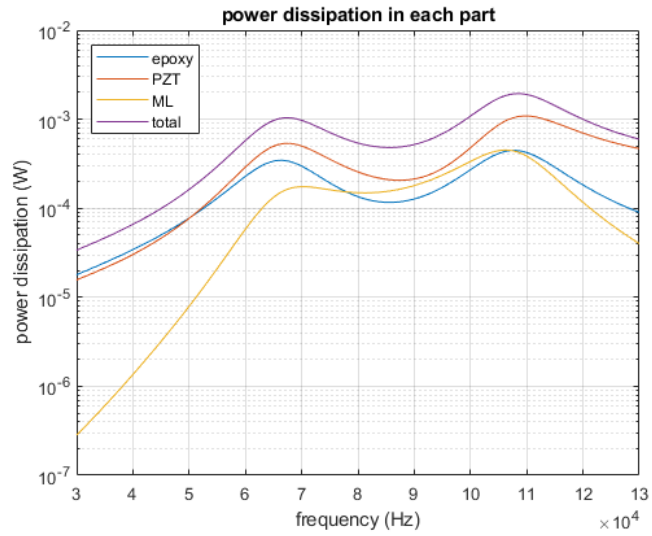


Fig. 4.15: Power dissipation within each material domain and the total power dissipation, all quantities defined in Eq. (3.25).

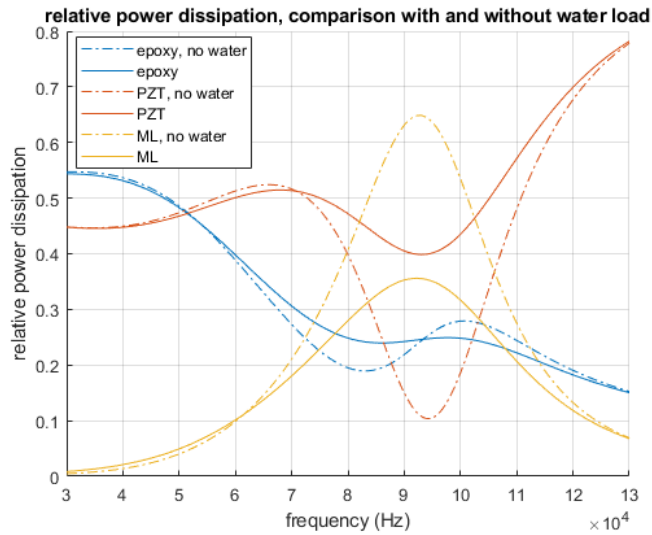


Fig. 4.16: Relative power dissipation within each material domain, all quantities defined in Eq. (3.26), for two cases: With (applicable to Fig. 4.15) and without water load (dot-dashed lines and "no water" appearing in legends for the latter case).

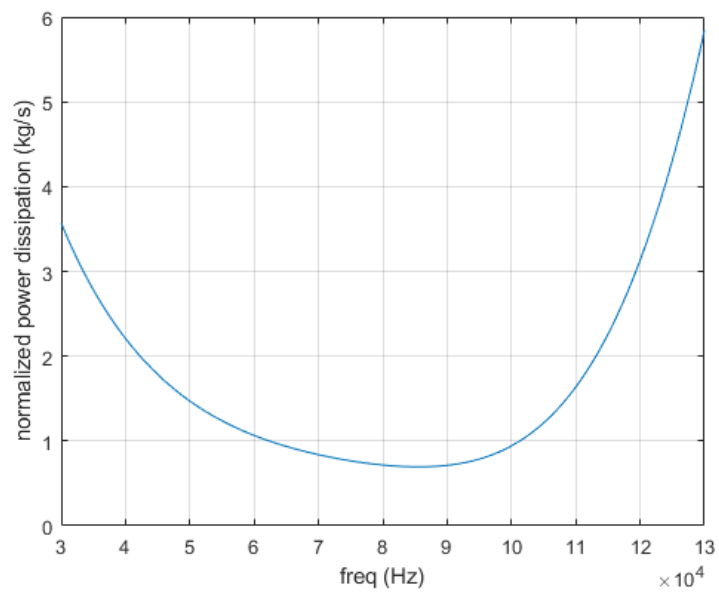


Fig. 4.17: Total power dissipation $P(f)$ as defined in Eq. (3.25) divided by the surface averaged absolute normal velocity squared $|v_{\perp, \text{avg}}|^2$ at the surface of the matching layer radiating into water. This gives a measure of radiation efficiency into water.

4.3 Steady-state heat transfer in 1-3 composite with electrodes, matching layer and water load

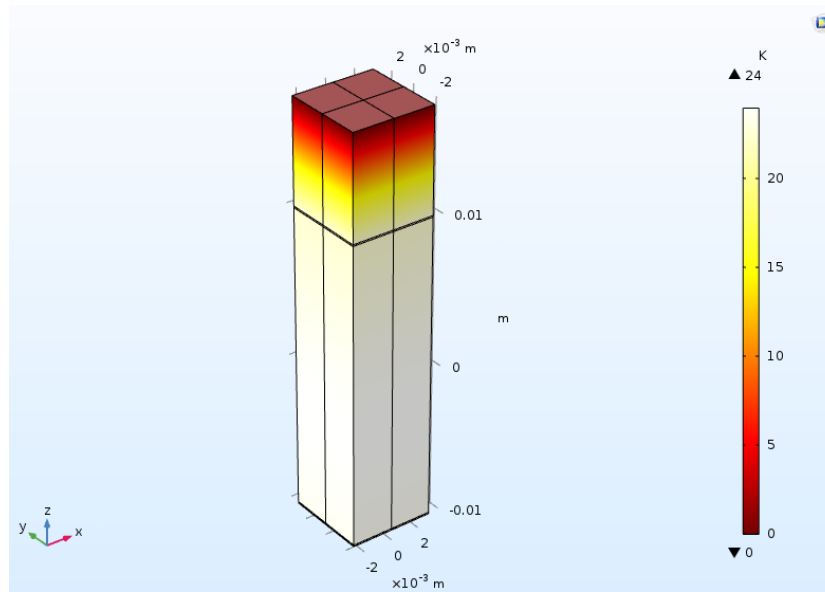


Fig. 4.18: Temperature rise at the outer surfaces of a unit cell, seen from the side. The absolute temperatures are given by the temperature rise in this Figure plus the water temperature of 15°C . The peak voltage was 200 V and the heat source used was that acquired at the frequency $f = 108\,400$ Hz of maximum total power dissipation.

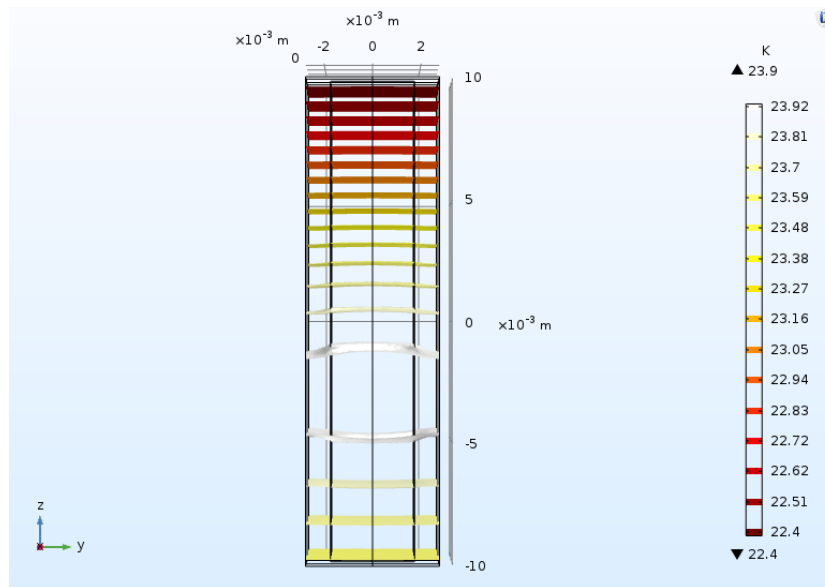


Fig. 4.19: Isocontours for the temperature increase in the composite, looking at a unit cell. The upper horizontal face ($z = 10$ mm) is connected to the upper electrode and the matching layer, while the lower face ($z = -10$ mm) is connected to the lower electrode. The absolute temperature at a given point is equal to the temperature rise in this Figure plus the water temperature of 15°C . The peak voltage was 200 V and the heat source used was that acquired at the frequency $f = 108\,400$ Hz of maximum total power dissipation.

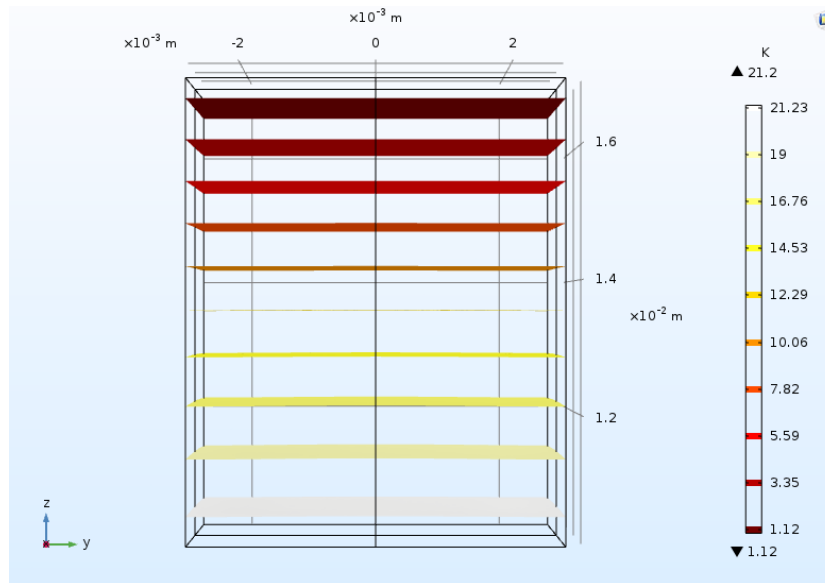


Fig. 4.20: Isocontours for the temperature increase in the matching layer, looking at a unit cell. The temperature increase is the lowest close to the upper face, where the constant temperature boundary condition was applied. The absolute temperature at a given point is equal to the temperature rise in this Figure plus the water temperature of 15°C . The peak voltage was 200 V and the heat source used was that acquired at the frequency $f = 108\,400 \text{ Hz}$ of maximum total power dissipation.

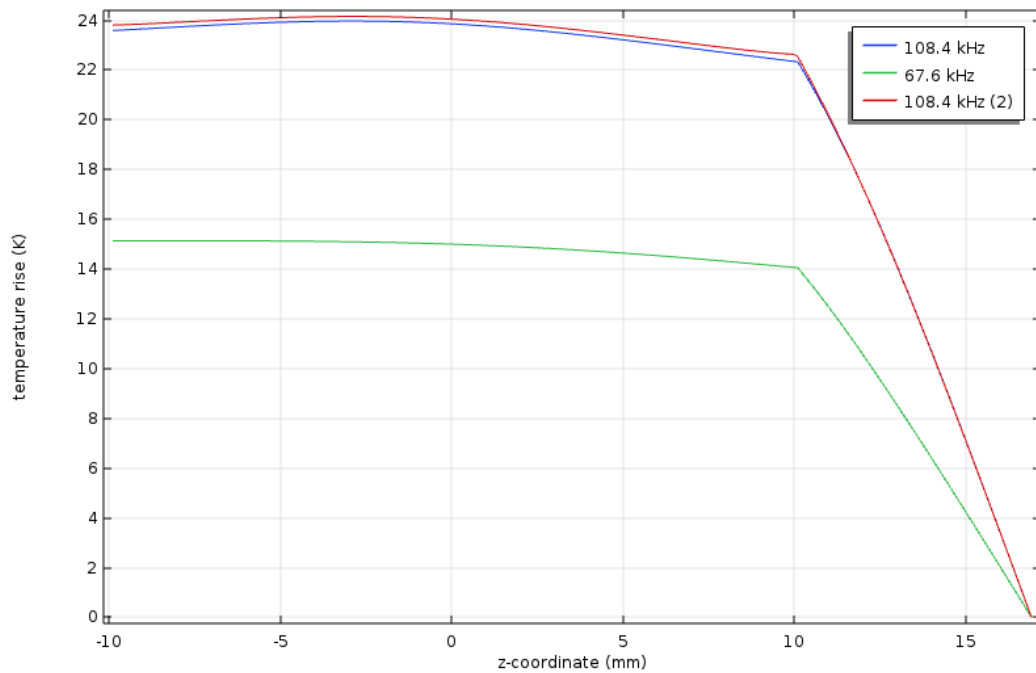


Fig. 4.21: Temperature rise along the center line of a unit cell, going through, from left to right, the PZT in the composite (-10 mm to 10 mm), the electrode between the composite and the matching layer (10 mm to 10.1 mm) and the matching layer. Three graphs are shown: The first, in blue, for heating at the frequency of maximum power dissipation, the second, in green, for heating at the frequency of local maximum of total power dissipation and the third and last, in red, for heating at same frequency as the blue curve but with the thermal conductivity of the electrode between the composite and the matching layer set to that of the composite. For references for the maxima, see Fig. 4.15. The absolute temperatures are given by the temperature rise in this Figure plus the water temperature of 15°C .

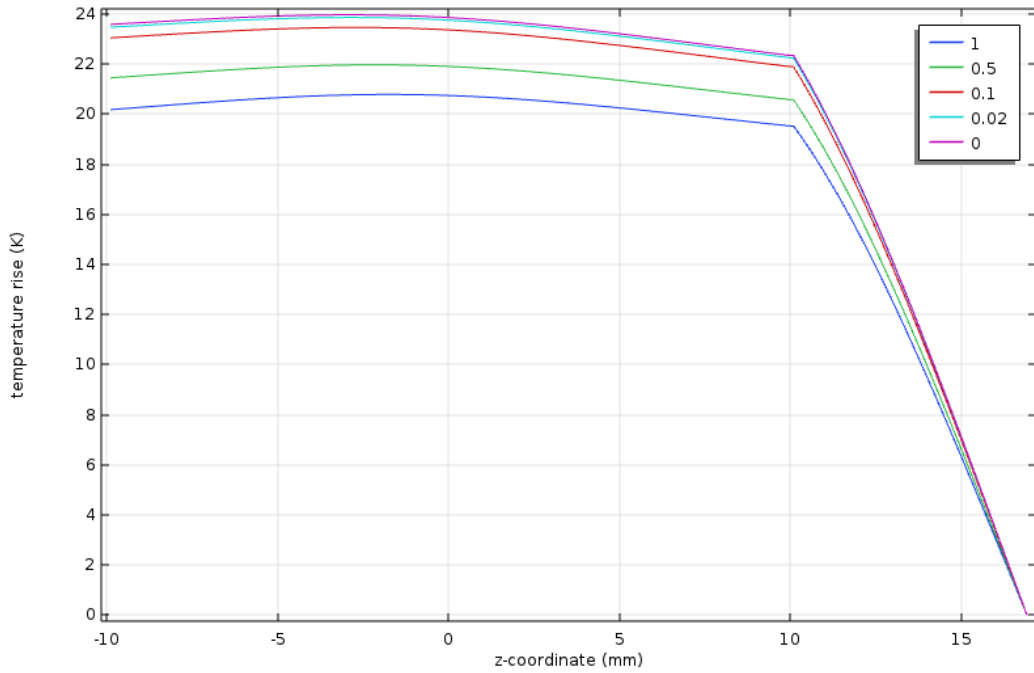


Fig. 4.22: Temperature rise along the center line of a unit cell, going through, from left to right, the PZT in the composite (-10 mm to 10 mm), the electrode between the composite and the matching layer (10 mm to 10.1 mm) and the matching layer. Here, an additional boundary condition has been applied to the lower surface of the lower electrode to approximate the effect of heat transfer by radiation from the electrode to the backing layer. The boundary condition, corresponding to thermal radiation emitted by a diffuse emitter, is given by Eq. (3.29). Five graphs are depicted with the legend indicating the emissivity ϵ_{th} of the copper surface used to obtain the results. The heat sources used corresponded to those for the frequency $f = 108\,400$ Hz (maximum power dissipation).

Chapter 5

Discussion

5.1 1-3 composites in vacuum

First, Table 4.1, showing the series f_s and parallel f_p resonance frequencies obtained in COMSOL compared with the corresponding frequencies \bar{f}_s and \bar{f}_p predicted by the effective medium model, will be discussed. Overall, there is good correspondence between the numerical and analytical model, the relative differences less than 10% in all cases. Based on the premises of the effective medium model as presented in Subsection 2.3.3, the effective medium model is expected to apply best to the quarter unit cells in COMSOL with the smallest rod sizes w_r because this yields the finest lateral scales. In contrast, the series resonance frequencies of the quarter unit cells with the coarsest lateral scale compared best to those of the effective medium model, see Table 4.1. Here, it is important to notice that the shortest wavelengths λ_{\min} in the composites of pillar size $w_r = 10.0$ mm range from 10.9 mm to 12.9 mm as given in Table 3.2, so these are indeed very coarse structures and certainly too coarse to be described well by the effective medium model. Therefore, this was an unexpected result. For the parallel resonance frequencies in Table 4.1, the best correspondence between the FEM analyses and the effective medium model was found for the intermediate rod size, namely $w_r = 6.0$ mm. Still, the resonance frequencies of the quarter unit cells with the smallest rod size are in good agreement with the effective medium model, especially the parallel resonance frequencies.

From Table 4.1, it is also clear that for a fixed volume fraction ν , the resonance frequencies f_s and f_p obtained by FEM modeling increased for decreasing rod size w_r . It was tested for composite no. 1 in Table 4.1 ($w_r = 3.5$ mm and $\nu = 0.4$) if further reduction of the rod size would give resonances at even higher frequencies. Decreasing the rod size stepwise and running new simulations at frequency intervals in the vicinity of the previously acquired resonance frequencies, it was found that the parallel and series resonance

frequencies converged to values within 1% of those obtained for a rod size of $w_r = 3.5$ mm. This means that a rod size of 3.5 mm and volume fraction of $\nu = 0.4$ should be sufficiently fine for comparison with the effective medium model for that volume fraction.

Next, consider the frequencies of maximum power dissipation in Fig. 4.1. As a consequence of Eq. (2.105), the frequency of maximum power dissipation should be equal to the frequency of maximum conductance, which was defined as the series resonance frequency f_s , for all composites. More importantly, as stated in Subsection 2.3.4, the power dissipation given by Eq. (2.105) is equivalent to Eq. (3.25). For the composite with rod size $w_r = 3.5$ mm and volume fraction $\nu = 0.4$, this correspondence is illustrated in Fig. 4.2 where the ratio $P(\omega)/(GV_0^2/2)$ is evaluated to unity within 1%.

A plot of the absolute value of the impedance as a function of frequency, $|Z(f)|$ (Eq. (3.15)), along with the phase angle $\delta(f)$, is presented in Fig. 4.3 for the same composite. For the lower frequencies, the phase angle is close to -90° as the resistance is close to zero here. According to the definitions of f_r and f_a in Subsection 2.3.2, the resonance occurs at ($f = f_r \approx 88\,400$ Hz) and as the phase angle vanishes the second time, the anti-resonance occurs ($f = f_a \approx 103\,600$ Hz). These values can also be found in Table 4.1.

Like f_s and f_p in Table 4.1, the fundamental thickness resonance frequency f_r and anti-resonance frequency f_a are found to increase with increasing volume fraction for a fixed rod size. In fact, comparison between f_r and f_s and between f_a and f_p shows that the resonance frequencies are identical (in terms of multiples of the sampling frequency) in almost all cases. This indicates that the absolute differences are too small to be accurately measured when using a sampling frequency of 400 Hz. For all of these frequencies in Figs. 4.1, though, the following can be said: They are shifted to higher frequencies for higher volume fractions because the composites stiffen as the PZT is stiffer than the epoxy.

Still discussing Fig. 4.1, consider the power dissipation per surface area P_A of the composites. For a fixed rod size w_r , the maximum loss can be seen to increase for increasing PZT volume fractions. In other words, as the volume fraction of epoxy reduces, this quantity becomes larger. As the epoxy volume of a unit cell decreases while the PZT volume remains the same, the PZT rod of the cell is loaded with less (piezoelectric inactive) mass and is able to vibrate more freely in a relative sense. Thus, the power dissipation

rises.

Now, change focus to Fig. 4.4, where the power dissipation per surface area P_A is plotted for composites with equal volume fraction ν . By Eq. (3.2), for a fixed ν , this situation is equivalent to $w_r/\Delta w_r$ being constant. Considering the values of the maxima, the relative difference between the three rod sizes grows as the volume fraction increases. This could not have been the case in the effective medium model as that model is independent of rod size. Although the sampling frequency could have been chosen lower near the peaks to predict the frequencies and values of the maxima more accurately, the relative differences might also reduce if the meshes are further refined. Although not performed here, the approach would be to reduce the mesh size further, run new simulations for a few frequencies centered around the resonance frequencies (to save time since only the maxima are relevant for this discussion) and check if the obtained relative differences were smaller.

Next, Fig. 4.5 depicting the relative power dissipation in the PZT and epoxy of the composites, as defined in Eq. (3.26), is discussed. Here, the results are compared in terms of varying volume fractions. For $w_r = 10$ mm and volume fraction $\nu = 0.4$, the epoxy and PZT curve have a maximum and minimum, respectively, at $f = 105\,200$ Hz. Investigating the total displacement amplitude $|\vec{\xi}|$, it is clear that a lateral resonance mode appears at that frequency. In Fig. 4.6, $|\vec{\xi}|$ is plotted for a 3×3 array of unit cells along with the spatial deformation at $f = 104\,800$ Hz, the latter hugely exaggerated for purposes of visualization. For reference, the displacement at resonance, $|\vec{\xi}(f_r)|$, is shown for the same composite and configuration of unit cells in Fig. 4.7, which displays a high degree of uniformity at the upper free surface. There are dominant peaks in the epoxy where the extension of the diagonals of neighbouring unit cells cross, suggesting a diagonal lateral resonance, discussed in Subsection 2.3.2 and Eq. (2.63). Using the shear wave velocity c_s of the epoxy as given in [20] and the epoxy width (equivalent to the rod spacing Δw_r) from Table 3.1, a fundamental diagonal resonance frequency of approximately $f_{t1} \approx 86$ kHz would be expected from Eq. (2.63). The impedance spectrum for the quarter cell is plotted in Fig. 4.8 and the second minimum ($f = 104\,800$ Hz) and maximum ($f = 106\,800$ Hz) correspond very well to the frequency of the observed lateral mode in Fig. 4.6. Despite the relatively large discrepancy with respect to Eq. (2.63), the pair of lateral resonance frequencies obtained for this rod spacing and volume fraction are

overall the frequencies closest to the respective frequency domains sampled. As discussed in Subsection 2.3.2, lateral modes close to the thickness mode is undesired for piezocomposite transducers operating in thickness mode. By Eq. (2.63), increasing the rod spacing Δw_r would shift the lateral mode to higher frequencies.

Continuing the discussion of Fig. 4.5, the relative power dissipation in the PZT is in most cases larger than the epoxy for the frequencies considered here. The exceptions are all rod sizes for $\nu = 0.8$ and of course $w_r = 3.5$ mm for which the lateral mode appears. Keeping the latter out of the discussion, there is a clear trend for the remaining 11 composites: For a fixed rod size w_r , the relative power dissipation in the epoxy increases as the volume fraction ν of PZT increases. Another important aspect for these composites is that, for the frequency domains considered, the power dissipation in the PZT dominates more the higher the frequency. Moreover, at resonance f_r , indicated in Fig. 4.5, there is no distinct change in the shape of the graphs.

In Fig. 4.9, the curves shown previously have been grouped in terms of the volume fraction of PZT in the respective composites. Except for $\nu = 0.4$, it holds that for a fixed volume fraction, a larger rod size yields a larger piezoelectric contribution to the total power dissipation. For the lowest volume fraction considered, the lateral mode makes comparison with the two other composites harder. As the frequency increases, the piezoelectric contribution for rod size 3.5 mm intercepts and grows beyond that for rod size 6.0 mm.

5.2 1-3 composite with electrodes, matching layer and water load

It is appropriate to start this discussion with the normalized electrical impedance plot $|Z(f)|/A$ in Fig. 4.10. In contrast to the 1-3 composites in vacuum just considered (except that with a lateral mode appearing), there are now two maxima and two minima in the impedance spectrum, and the phase angle neither vanishes at the minima nor the maxima. The first fact is explained by the inclusion of the matching layer: This added mass lowers the frequency of the resonance of the composite (denoted by f_{r1}, f_{a1} in the following) with

Table 5.1: Overview of extrema of the electric impedance $|Z(f)|$ in Fig. 4.10. In the last column, comp. is short for composite and ML is short for matching layer.

symbol	frequency (Hz)	description	resonance of
f_{r1}	64 000	1 st minimum of $ Z(f) $	comp.
f_{a1}	78 400	1 st maximum of $ Z(f) $	comp.
f_{r2}	102 000	2 nd minimum of $ Z(f) $	comp. and ML
f_{a2}	117 600	2 nd maximum of $ Z(f) $	comp. and ML

respect to the free composite case and, together with the composite, gives rise to a combined resonance at a higher frequency (denoted by f_{r2}, f_{a2} in the following). The second observation is a consequence of the water load: The reactance $X(f)$ remains non-zero at resonance. The values of the resonance frequencies are given in Table 5.1. Another important remark is that the modulus of the impedance drops quite heavily in between f_{r1} and f_{r2} . This is due to the choice of characteristic acoustic impedance Z_{ML} of the matching layer, picked to transfer power most efficiently as discussed in Subsection 3.3.1. The maximally flat response for one matching layer is obtained when the characteristic acoustic impedance of the matching layer is equal to $(Z_{comp}^{1/3} Z_{water}^{2/3})^{1/2}$ [23], Z_{comp} (Z_{water}) denoting the characteristic acoustic impedance of the composite (water).

In the next Figure, Fig. 4.11, the power dissipation density P_d is plotted at $f = f_{r2}$ for a cross section in the yz -plane ($x = 0$) through the center of one unit cell. Due to symmetry, this is equivalent with $y = 0$. f_{r2} is in fact also the frequency of maximum total power dissipation $P(\omega)$ by Eq. (3.10). The upper portion of the plot shows the power dissipation in the matching layer and below, the PZT appears in the middle with epoxy on both sides. It is mentioned again that the electrodes are assumed to be lossless, so these will not be considered in this discussion.

The values of the power dissipation density are clearly the highest in the PZT, increasing from the top and bottom towards the middle of the rod. However, the maximum is shifted towards the lower half due to the loading of the matching layer and water. What can also be seen is negative power dissipation density, which is most significant in the green areas in the upper portion of the PZT and at the two bright yellow "points" in the opposite end.

This effect can simply not have roots in the physical reality as this would mean a power gain, so it must be an artifact of the FEM modeling. Further investigation was carried out and now considering a quarter cell for better visualization, the elements which have at least one node where the power dissipation density is negative were plotted in Fig. 4.12. The Figure reveals critical lines along the material borders between the PZT and epoxy at the top and bottom side of the composite where the power dissipation density is the most negative. Also note that the quantity reaches below zero only within the PZT.

To give a measure of how large the quantity of negative power dissipation density was, the negative portion of the power dissipation was integrated over the volume of the PZT and divided by the power dissipation in the composite $P_{\text{PZT}} + P_e$ as defined in Eq. (3.13) to form a ratio. To see how the ratio changed for coarser and finer meshes, one coarser and one finer mesh were generated. Fig. 4.13 shows the absolute value of the introduced ratio for three different meshes, labeled mesh1, mesh2 and mesh3 with their approximate run times in hours and approximate number of elements labeled. This indicates that mesh1 was the coarsest mesh and that mesh3 was the finest mesh. mesh2 was used to produce Fig. 4.11. The ratio decreases by a few percent for the finest mesh. However, how much does the total power dissipation change? Fig. 4.14 displays the total power dissipation normalized with respect to mesh2. As the power dissipation of the finest mesh (mesh3) differs from that of mesh2 only by around 1% at most and the computational effort increases significantly, mesh2 is kept for the remaining results in this discussion of the composite with matching layer and water load.

The power dissipation in the lossy materials over a quarter unit cell together with the the total power dissipation is plotted in Fig. 4.15. At low frequencies, the dissipation in the matching layer is clearly negligible, while at high frequencies, the PZT holds the largest contribution. The first and second maximum of total power dissipation occur at a higher frequency with respect to the resonance frequency f_{r1} and f_{r2} , respectively, of Table 5.1. The next Figure Fig. 4.16 displays the relative power dissipations as given in Eq. (3.14). To interpret the results, it was helpful to compare these quantities to the corresponding quantities obtained from a simulation without the water load.

First, it is interesting to note that the differences between the two different

scenarios seem to vanish towards both ends of the frequency domain and that the largest changes occur at the frequency interval between the two resonances. Both observations are probably explained by the fact that the resonance behaviour dies out towards the ends of the spectrum. Without the water load, the local minimum and local maximum of the epoxy contribution Π_e is more distinct, appearing relatively flat with water. The largest changes are seen in the matching layer and PZT for frequencies higher than the center frequency of the domain ($f = 80\,000$ Hz). The matching layer clearly dominates when it is not loaded with water while the PZT gives the largest contribution in the other case. At the maximum of relative power dissipation in the matching layer, the quantity increases by roughly 0.3 when the water load is disregarded while that of the PZT decreases by about the same amount.

Last but not least, the power dissipation $P(f)$ normalized with respect to the squared absolute value of the average particle velocity at the upper matching layer surface $|v_{\perp,\text{avg}}|^2$, is plotted in Fig. 4.17. As the sound power emitted into water is proportional to $|v_{\perp,\text{avg}}|^2$, this gives a measure of the ratio of the losses to the radiated sound power, so this is measure of efficiency. For this simplified model of a transducer, the plot suggests that the structure emits most efficiently close to the anti-resonance of the piezocomposite, f_{a1} .

5.3 Steady-state heat transfer in 1-3 composite with electrodes, matching layer and water load

This discussion concludes the last part of the simulations on steady-state heat transfer in the composite with electrodes, matching layer and water load. The temperature rise for the outer surfaces of a unit cell is shown in Fig. 4.18 for the frequency of maximum total power dissipation, found to be 108 400 Hz by inspection of Fig. 4.15. Notice first that the temperature increase at the upper face of the matching layer is zero. This is as expected as this is where the constant temperature boundary condition was applied, see Fig. 3.5. The largest temperature increase of about 24 K was found to be in the composite and the distribution looks fairly homogeneous with respect to

the thickness direction (z -coordinate in the plot). To be able to tell this more accurately, isocontour plots of the temperature increase were generated, one for the composite (Fig. 4.19) and one for the matching layer (Fig. 4.20). Fig. 4.19 displaying the composite makes it clear that not only is the variation in temperatures less than 2 K throughout this part, but the distribution is also independent of the lateral coordinates except close the warmest regions. For the matching layer, the temperature is similarly homogeneous along planes normal to the thickness direction. All in all, these Figures indicate that with the steady-state approach, spatial variations of the heat source across the epoxy and PZT in the composite and in the matching layer (as seen in Fig. 4.11) are hard to spot in the resulting temperature distribution.

Fig. 4.21 shows the temperature increase along the center line of the unit cell, running through, from the bottom to the top, the composite (z within -10.0 mm to 10.0 mm), the upper electrode (z within 10.0 mm to 10.1 mm) and the matching layer. Three cases are considered: The resulting temperature distribution by heating at the frequency of global maximum total power dissipation (blue), the distribution at the frequency of the first local maximum (green) and the distribution by heating at frequency of maximum power dissipation but this time with the thermal conductivity of the upper electrode equal to that of the matching layer. The last scenario was made to see what role that electrode plays in distributing the heat. As is illustrated, the effect is marginal at steady-state. In Subsection 3.3, the motivation to include the electrodes in the first place was to see how they affected the temperature distribution in the composite and matching layer. Now seeing that the changes are negligible when the high thermal conductive property of the electrodes is left out of the simulation, the electrodes may be safely disregarded from such analysis.

It was also found that the maximum temperature rise was the highest at the frequency of maximum total power dissipation (frequency 108 400 Hz). The temperature distribution in the matching layer is for all three cases linear to a very high degree with respect to the z -coordinate, and since the distribution is in very good approximation transversely homogeneous as discussed in the paragraph above, the temperature increase in the matching layer could in principle be given in terms of the z -coordinate and the temperatures on either sides only. In fact, this is also the same distribution as obtained by considering purely conductive steady-state heat transfer through a rectangular slab of uniform cross section and thermal conductivity, with one end held

at a constant temperature and the opposite end held at a different constant temperature [24].

Now, the assumption about thermal radiation made in Subsection 3.4.1 will be checked. To remind the reader, it was assumed that there would be negligible reductions in temperature increase caused by thermal radiation from the lower electrode into the backing layer. The steady-state heat transfer simulation was performed again with one change: The lower surface of the lower electrode was now not only transferring heat to the backing layer by convection but also by radiation through the boundary condition given in Eq. (3.29). Under the assumption that the electrode surface was a diffuse emitter and that all radiated thermal energy was lost to the backing layer, four different emissivities ϵ_{th} were considered, and the resulting temperature increases through the center line of the unit cell (similar to Fig. 4.21) were compared. The distributions are shown in Fig. 4.22 with the applied emissivities ϵ_{th} displayed in the legend. The fifth graph, with zero emissivity, is equivalent with no radiation. By this somewhat simplified approach, it becomes clear that as long as the copper electrode has an emissivity of less than about 0.5, the assumption is valid, whereas for higher emissivities, radiation could give a significant reduction ($> 10\%$) of the temperature rise and should be modeled. In general, the emissivity of a metal such as copper is strongly dependent on the surface treatment [24].

Lastly, it is necessary to address the thermal material parameters used and the uncertainties of the material parameters. The thermal conductivity k used for the PZT was found in the data sheet of the manufacturer [18]. However, those for the epoxy and matching layer were not available, so they were assumed based on typical values for similar materials. For more accurate steady-state heat transfer analysis, material-specific thermal conductivities should have been used. In addition, the heat transfer coefficient h was assumed for still air in the backing layer, which seems reasonable. Regarding the uncertainties in material parameters, a relative uncertainty of 10% was given for the material coefficients of the PZT in [19]. Uncertainties of the material coefficients of the remaining materials were not available and may be assumed similar.

Chapter 6

Conclusion

In this thesis, FEM models of thickness mode 1-3 piezoelectric composites with square piezoelectric rods were created to investigate the heat generation and temperature increase when the composites were driven by a sinusoidal voltage. The work was performed in three stages.

First, 12 different composites, showing a variety of PZT volume fractions and pillar aspect ratios, were considered. Dielectric, mechanical and piezoelectric losses were specified in terms of complex material coefficients for the PZT, while the epoxy was modeled as a linear isotropic elastic medium with mechanical losses determined by its mechanical quality factor. Due to limited computational resources, quarter unit cell models of the composites were simulated with symmetric boundary conditions, giving infinite periodic structures along the lateral directions. The finite element modeling was conducted over frequency domains covering the fundamental thickness resonance and anti-resonance of the composites. The normalized power dissipation in the composites and the relative contribution from the PZT and epoxy were compared for fixed rod sizes and fixed PZT volume fractions. In one case, a diagonal lateral mode in the epoxy appeared close to the anti-resonance frequency. The main outcome at this stage was that the relative power dissipation for frequencies close to the lateral resonance frequency was dominated by the epoxy.

Second, a quarter-wavelength matching layer with characteristic acoustic impedance chosen for maximum power transmission into a water load was added to one of the composites from the previous step. Losses in the matching layer were specified through the complex longitudinal and shear wave velocities. It was found that the most efficient power transmission into water occurred over a frequency interval located between the resonance of the composite and the combined resonance of the composite and the matching layer. On that same frequency interval, the relative power dissipation in the epoxy peaked while that in the PZT dropped.

Finally, the power dissipation density obtained from the previous FEM model was used as the heat source in a steady-state heat transfer model of the same structure. With the transducer stack submerged in sea water at constant temperature and the composite transferring heat by convection to the air backing layer, the temperature distribution obtained in the matching layer and the composite was found to be practically homogeneous in planes normal to the thickness direction. The maximum temperature increase was found to be approximately 24 K for a peak voltage of 200 V.

Further work could include simulations on finite-sized composites with matching layers and water load. This would require much more computational effort and may be convenient to run on a cluster. In addition, Holland's expression for the power dissipation density in a piezoelectric may be decomposed into several terms according to Eq. (2.49). It would be interesting to see how much each term contributes at lateral and fundamental thickness resonance frequencies. Last but not least, the sampled frequency domain could be expanded to include higher order resonances.

Appendix A

Piezoelectric equations and inter-relations

One of the four pairs of piezoelectric equations has already been presented in Eqs. (2.32) and (2.33). This will be used as a basis to derive the three remaining pairs of piezoelectric equations.

First, consider \vec{T} (Voigt notation for the stresses, see Section 2.1.1) and \vec{E} as independent variables. Rewriting Eq. (2.33) yields

$$\begin{aligned}\vec{E} &= (\boldsymbol{\epsilon}^S)^{-1} \vec{D} - (\boldsymbol{\epsilon}^S)^{-1} \mathbf{e} \vec{S} \\ &\equiv \boldsymbol{\beta}^S \vec{D} - \mathbf{h} \vec{S}.\end{aligned}\tag{A.1}$$

Inserting this final Equation into Eq. (2.32) gives

$$\begin{aligned}\vec{T} &= (\mathbf{c}^E + \mathbf{e}^t \mathbf{h}) \vec{S} - \mathbf{e}^t \boldsymbol{\beta}^S \vec{D} \\ &\equiv \mathbf{c}^D \vec{S} - \mathbf{h}^t \vec{D}.\end{aligned}\tag{A.2}$$

These two Equations are the piezoelectric equations on the \mathbf{h} -form.

Second, take \vec{S} (Voigt notation for the strain, see Section 2.1.1) and \vec{D} as independent variables. Solving Eq. (2.32) for \vec{S} results in

$$\begin{aligned}\vec{S} &= (\mathbf{c}^E)^{-1} \vec{T} + (\mathbf{c}^E)^{-1} \mathbf{e}^t \vec{E} \\ &\equiv \mathbf{s}^E \vec{T} + \mathbf{d}^t \vec{E}.\end{aligned}\tag{A.3}$$

Insertion in Eq. (2.33) then gives

$$\begin{aligned}\vec{D} &= \mathbf{e} \mathbf{s}^E \vec{T} + (\mathbf{e} \mathbf{d}^t + \boldsymbol{\epsilon}^S) \vec{E} \\ &\equiv \mathbf{d} \vec{T} + \boldsymbol{\epsilon}^T \vec{E}.\end{aligned}\tag{A.4}$$

One has acquired the piezoelectric equations on the \mathbf{d} -form.

Finally, consider \vec{S} and \vec{E} as independent variables. Then, rewriting Eq. (A.2) yields

$$\begin{aligned}\vec{S} &= (\mathbf{c}^D)^{-1} \vec{T} + (\mathbf{c}^D)^{-1} \mathbf{h}^t \vec{D} \\ &\equiv \mathbf{s}^D \vec{T} + \mathbf{g}^t \vec{D}\end{aligned}\tag{A.5}$$

The previous Equation inserted into Eq. (A.1) implies

$$\begin{aligned}\vec{E} &= -\mathbf{h} \mathbf{s}^D \vec{T} + (\boldsymbol{\beta}^S - \mathbf{h} \mathbf{g}^t) \vec{D} \\ &\equiv -\mathbf{g} \vec{T} + \boldsymbol{\beta}^T \vec{D}.\end{aligned}\tag{A.6}$$

These Equations are known as the piezoelectric equations on the \mathbf{g} -form.

Note that Eqs. (A.1) - (A.6) do not give all possible interrelations. However, one sees that there are two types of relations falling out of this kind of manipulation. First, there are equations where two piezoelectric coefficients are expressed in terms of one dielectric or one mechanical coefficient. Second, there are relations between the constant \vec{D} and constant \vec{E} mechanical coefficients and between the constant \vec{S} and constant \vec{T} dielectric coefficients. Below, all interrelations are given for completeness.

$$\mathbf{d} = \mathbf{e} \mathbf{s}^E = \boldsymbol{\epsilon}^T \mathbf{g}\tag{A.7}$$

$$\mathbf{e} = \mathbf{d} \mathbf{c}^E = \boldsymbol{\epsilon}^S \mathbf{h}\tag{A.8}$$

$$\mathbf{g} = \mathbf{h} \mathbf{s}^D = \boldsymbol{\beta}^T \mathbf{d}\tag{A.9}$$

$$\mathbf{h} = \boldsymbol{\beta}^S \mathbf{e} = \mathbf{g} \mathbf{c}^D\tag{A.10}$$

$$\mathbf{c}^D - \mathbf{c}^E = \mathbf{e}^t \mathbf{h}\tag{A.11}$$

$$\mathbf{s}^E - \mathbf{s}^D = \mathbf{g}^t \mathbf{d}\tag{A.12}$$

$$\boldsymbol{\beta}^S - \boldsymbol{\beta}^T = \mathbf{h} \mathbf{g}^t\tag{A.13}$$

$$\boldsymbol{\epsilon}^T - \boldsymbol{\epsilon}^S = \mathbf{e} \mathbf{d}^t\tag{A.14}$$

Appendix B

Material properties

PZT

Material properties as given in [14] unless otherwise stated.

$$\begin{aligned}s_{11}^E &= (1.12 - 0.01i) \cdot 10^{-11} \text{ m}^2\text{N}^{-1} \\s_{12}^E &= (-0.33 + 0.01i) \cdot 10^{-11} \text{ m}^2\text{N}^{-1} \\s_{13}^E &= (-0.70 + 0.02i) \cdot 10^{-11} \text{ m}^2\text{N}^{-1} \\s_{33}^E &= (1.25 - 0.04i) \cdot 10^{-11} \text{ m}^2\text{N}^{-1} \\s_{44}^E &= (3.25 - 0.16i) \cdot 10^{-11} \text{ m}^2\text{N}^{-1}\end{aligned}$$

$$\begin{aligned}\epsilon_{11}^T &= (1.43 - 0.86i) \cdot 10^{-8} \text{ Fm}^{-1} \\ \epsilon_{33}^T &= (0.859 - 0.0024i) \cdot 10^{-8} \text{ Fm}^{-1}\end{aligned}$$

$$\begin{aligned}d_{13} &= (-94.8 - 0.3i) \cdot 10^{-12} \text{ CN}^{-1} \\d_{33} &= (201 - 2.2i) \cdot 10^{-12} \text{ CN}^{-1} \\d_{15} &= (422 - 210i) \cdot 10^{-12} \text{ CN}^{-1}\end{aligned}$$

$$\rho = 7500 \text{ kgm}^{-3}$$

From [18]:

$$k = 1.2 \text{ Wm}^{-1}\text{K}^{-1}$$

Epoxy

Material properties as given in [20] unless otherwise stated.

$$E = 0.63 \cdot 10^{10} \text{ Nm}^{-2}$$

$$\sigma = 0.30$$

$$\rho = 1200 \text{ kgm}^{-3}$$

$$Q_m = 24.5$$

$$\tan \delta_\epsilon = 0.005$$

$$\epsilon' / \epsilon_0 = 4.21$$

Assumed:

$$k = 0.125 \text{ Wm}^{-1}\text{K}^{-1}$$

Matching layer

Material properties as given in Table 3 in [21] unless otherwise stated.

$$c_l = 2416.9 \text{ ms}^{-1}$$

$$c_s = 1195.5 \text{ ms}^{-1}$$

$$\alpha_l = 78 \text{ dBm}^{-1}$$

$$\alpha_s = 208 \text{ dBm}^{-1}$$

$$\rho = 1990.6 \text{ kgm}^{-3}$$

characteristic acoustic impedance $Z = 4.81 \text{ Mrayls}$ ($= Z_{ML}$ in Eq. (3.22))

Also given:

$$f_0 = 500 \text{ kHz}$$
 (used in Eq. (3.23))

Assumed:

$$k = 0.04 \text{ Wm}^{-1}\text{K}^{-1}$$

Electrodes (copper)

Material properties given by the COMSOL Multiphysics material library.

$$\rho = 8960 \text{ kgm}^{-3}$$

$$E = 110 \cdot 10^9 \text{ Nm}^{-2}$$

$$\sigma = 0.35$$

$$k = 400 \text{ Wm}^{-1}\text{K}^{-1}$$

Water

Material properties as given in the Appendix in [1].

$\rho = 1026 \text{ kgm}^{-3}$, $c = 1500 \text{ ms}^{-1}$ ($\rho c = Z_{\text{water}}$ in Eq. (3.22))

Air

heat transfer coefficient $h = 5 \text{ Wm}^{-2}\text{K}^{-1}$

References

- [1] John L. Butler and Charles H. Sherman. *Transducers and arrays for underwater sound*. Springer, 2016.
- [2] Daniel Royer. *Elastic waves in solids : 1 : Free and guided propagation*, volume 1. Springer, Berlin, 2000.
- [3] Wallace Arden Smith and Bertram A. Auld. Modeling 1-3 composite piezoelectrics: thickness-mode oscillations. *IEEE transactions on ultrasonics, ferroelectrics, and frequency control*, 38(1):40–47, 1991.
- [4] Xuecang Geng and Q.M. Zhang. Resonance modes and losses in 1-3 piezocomposites for ultrasonic transducer applications. *Journal of applied physics*, 85(3):1342–1350, 1999.
- [5] Wenkang Qi and Wenwu Cao. Finite element analysis and experimental studies on the thickness resonance of piezocomposite transducers. *Ultrasonic imaging*, 18(1):1–9, 1996.
- [6] Comsol multiphysics web page. <https://www.comsol.com/>. Accessed: June 1, 2018.
- [7] Bjørn A.J. Angelsen. *Ultrasound imaging : waves, signals, and signal processing : Vol. 1 : Basic principles, wave generation, propagation, and beamforming in homogeneous tissue*, volume Vol. 1. Emantec AS, Trondheim, 2000.
- [8] Zinoviy Nazarchuk, Valentyn Skalskyi, and Oleh Serhiyenko. *Acoustic Emission: Methodology and Application*. Springer, 2017.
- [9] Jose Pujol. *Elastic wave propagation and generation in seismology*. Cambridge University Press, 2003.
- [10] Richard Holland. Representation of dielectric, elastic, and piezoelectric losses by complex coefficients. *IEEE transactions on Sonics and Ultrasonics*, 14(1):18–20, 1967.
- [11] David J. Griffiths. *Introduction to electrodynamics*. AAPT, 2005.

- [12] Ahmad Safari and E. Koray Akdogan. *Piezoelectric and acoustic materials for transducer applications*. Springer Science & Business Media, 2008.
- [13] Per C. Hemmer. *Faste stoffers fysikk*. Tapir Forlag, 1987.
- [14] Stewart Sherrit and Binu K. Mukherjee. Characterization of piezoelectric materials for transducers. *arXiv preprint arXiv:0711.2657*, 2007.
- [15] Ronald E. McKeighen. Design guidelines for medical ultrasonic arrays. In *Medical Imaging 1998: Ultrasonic Transducer Engineering*, volume 3341, pages 2–19. International Society for Optics and Photonics, 1998.
- [16] Anne-Christine Hladky-Hennion and Jean-Noël Decarpigny. Finite element modeling of active periodic structures: Application to 1–3 piezocomposites. *The Journal of the Acoustical Society of America*, 94(2):621–635, 1993.
- [17] John A. Hossack and Gordon Hayward. Finite-element analysis of 1-3 composite transducers. *IEEE transactions on ultrasonics, ferroelectrics, and frequency control*, 38(6):618–629, 1991.
- [18] Harris Corporation. *Electro-ceramic products and materials specification*, 2017.
- [19] Ribal Georges Sabat, Binu K. Mukherjee, Wei Ren, and Guomao Yang. Temperature dependence of the complete material coefficients matrix of soft and hard doped piezoelectric lead zirconate titanate ceramics. *Journal of Applied Physics*, 101(6):064111, 2007.
- [20] Kei C. Cheng, Helen L.W. Chan, Chung L. Choy, Qingrui Yin, Hasou Luo, and Zhiwen Yin. Single crystal pmn-0.33 pt/epoxy 1-3 composites for ultrasonic transducer applications. *IEEE transactions on ultrasonics, ferroelectrics, and frequency control*, 50(9):1177–1183, 2003.
- [21] Alexandre Trogé, Richard L. O’Leary, Gordon Hayward, Richard A. Pethrick, and Anthony J. Mullholland. Properties of photocured epoxy resin materials for application in piezoelectric ultrasonic transducer matching layers. *The Journal of the Acoustical Society of America*, 128(5):2704–2714, 2010.

- [22] D. Thomas, D.D. Ebenezer, and Sivakumar M. Srinivasan. Power dissipation and temperature distribution in piezoelectric ceramic slabs. *The Journal of the Acoustical Society of America*, 128(4):1700–1711, 2010.
- [23] Charles S. Desilets, John D. Fraser, and Gordon S. Kino. The design of efficient broad-band piezoelectric transducers. *IEEE Transactions on sonics and ultrasonics*, 25(3):115–125, 1978.
- [24] P.S. Ghoshdastidar. *Heat Transfer (2nd Edition)*. Oxford University Press, 2012.